

# Olenekian sulfur isotope records: Deciphering global trends, links to marine redox changes and faunal evolution

Oluwaseun Edward<sup>a,\*</sup>, Jorge E. Spangenberg<sup>a</sup>, Marc Leu<sup>b</sup>, Charline Ragon<sup>c</sup>, Sandrine Le Houedec<sup>d</sup>, Aymon Baud<sup>e</sup>, Hugo Bucher<sup>b</sup>, Torsten Vennemann<sup>a</sup>

<sup>a</sup> Institute of Earth Surface Dynamics, University of Lausanne, Géopolis, CH-1015 Lausanne, Switzerland

<sup>b</sup> Paläontologisches Institut der Universität Zürich, Karl-Schmid-Strasse 4, 8006 Zürich, Switzerland

<sup>c</sup> Group of Applied Physics and Institute for Environmental Sciences, University of Geneva, Boulevard Carl Vogt 66, 1205 Geneva, Switzerland

<sup>d</sup> Department of Earth Sciences, Université de Genève, Rue des Maraichers 13, CH-1205 Genève, Switzerland

<sup>e</sup> Institute of Earth Sciences, University of Lausanne, Géopolis, CH-1015 Lausanne, Switzerland

## ARTICLE INFO

Editor: Dr. Karen Johannesson

### Keywords:

Sulfur isotopes  
SSB  
Sulfur cycle  
Seawater sulfate  
Marine redox  
CAS

## ABSTRACT

The sulfur (S) isotope composition of carbonate associated sulfate (CAS) in carbonate rocks has been used to assess variations in paleo-oceanographic redox conditions and its relationship to biotic changes in Earth's history, including the Smithian – Spathian transition. However, previous CAS studies of the Olenekian are mostly based on nearshore continental shelf sections and report highly variable  $\delta^{34}\text{S}$  values mostly offset from those of contemporaneous evaporites, casting doubt on the utility of the CAS proxy during this interval. The current study presents new CAS isotopic data from three well-dated carbonate successions which were deposited in continental shelf (Qiakong) and offshore marine (Wadi Musjah and Jebel Aweri) environments during the Olenekian (Smithian – Spathian). The aim of the study was to constrain the temporal and spatial variations in sulfur cycling and its relation to marine redox and faunal changes across the Smithian – Spathian transition (ca. 250.5–248.8 Ma). The CAS dataset is complemented by rare earth element (REE) concentration data and thin section petrography. Using a suite of optical and geochemical techniques, the preservation of near-primary CAS isotopic information in the studied samples is evaluated. Results indicate that of the three sections investigated, the offshore sections mostly preserve near-primary marine sulfate S-isotope compositions while the continental shelf Qiakong section suffers from post-depositional alteration of CAS. Comparisons of our new, as well as previously published CAS  $\delta^{34}\text{S}$  data, with the evaporite  $\delta^{34}\text{S}$  record suggests that although Olenekian CAS  $\delta^{34}\text{S}$  values may have been modified by diagenetic processes, a global and primary seawater  $\delta^{34}\text{S}$  trend can be delineated as follows: seawater  $\delta^{34}\text{S}$  values increased across the middle Smithian and Smithian – Spathian boundary (SSB). Based on our new CAS data, this increase was in the order of 9 ‰ over ca. 1.14 million years. Other short-term variability in the CAS  $\delta^{34}\text{S}$  record most likely reflects diagenetic processes. The middle Smithian to SSB  $\delta^{34}\text{S}$  increase is attributed to a global increase in microbial sulfate reduction and pyrite burial associated with decreasing ocean dissolved oxygen during this time. Calculations of the rate of sulfur cycling and box modeling constraints indicate that Olenekian marine sulfur cycle perturbations occurred while the seawater sulfate reservoir only had between 10 and 25% of the modern marine sulfate inventory. Furthermore, results from the current study suggest that variations in ocean dissolved oxygen levels, inferred from the  $\delta^{34}\text{S}$  and REE data, are not consistently correlated with nektonic faunal changes during the Olenekian in the studied sections. As such, faunal turnover during the Olenekian is unlikely to be explained exclusively by abiotic factors such as ocean-atmosphere oxygenation levels.

## 1. Introduction

The sulfur (S) isotope composition of marine sulfate is a widely used

proxy for reconstructing changes in the oxygen content of the ocean-atmosphere system, marine redox evolution, and the chemical composition of the ocean (Holser and Kaplan, 1966; Claypool et al., 1980;

\* Corresponding author.

E-mail address: [oluwaseun.edward@unil.ch](mailto:oluwaseun.edward@unil.ch) (O. Edward).

<https://doi.org/10.1016/j.chemgeo.2024.121984>

Received 12 October 2023; Received in revised form 31 January 2024; Accepted 7 February 2024

Available online 10 February 2024

0009-2541/© 2024 The Authors. Published by Elsevier B.V. This is an open access article under the CC BY license (<http://creativecommons.org/licenses/by/4.0/>).

Berner, 1987; Strauss, 1997; Kampschulte et al., 2001; Bottrell and Newton, 2006; Turchyn and DePaolo, 2019). The sulfate ion ( $\text{SO}_4^{2-}$ ) is the second most abundant anion in seawater (Millero, 2013) and serves as an electron acceptor for the anaerobic breakdown of organic matter (OM) by microbes in marine systems (Habicht and Canfield, 1996; Bottrell and Newton, 2006; Jørgensen et al., 2019). This process, commonly referred to as microbial sulfate reduction (MSR), is the most important anaerobic pathway for OM respiration in the oceans (Jørgensen, 1982). MSR produces reduced sulfur ( $\text{HS}^-$ ), which in the presence of reactive iron, forms pyrite (Strauss, 1997) and together with organic carbon, is subsequently buried in marine sediments. This burial process leaves oxidized products in the ocean-atmosphere system and impacts the oxygen cycle (Berner, 1987; Halevy et al., 2012). As such, the marine sulfur cycle is connected to that of carbon and oxygen and impacts the oxygenation state of the oceans and atmosphere and hence, the ability of Earth's marine environments to support biological function

and diversity. Variations in the S-isotope composition of seawater sulfate are governed by relative changes in input and output fluxes of marine sulfur, which involve the transfer of sulfur between different reservoirs (Strauss, 1997; Bottrell and Newton, 2006; Gill et al., 2007). Specifically, the input fluxes of marine sulfur (i.e., sulfide weathering, volcanic degassing) are usually  $^{34}\text{S}$ -depleted relative to the marine sulfate pool, resulting in decreased seawater  $\delta^{34}\text{S}$  as these input fluxes increase (Wortmann et al., 2001). In contrast, the output fluxes such as sulfide burial and microbial sulfate reduction (MSR) preferentially deplete  $^{32}\text{S}$  in the marine sulfate pool, resulting in a  $^{34}\text{S}$  enrichment of seawater sulfate (Kah et al., 2004; Stebbins et al., 2019b). Consequently, investigating the variations in the S-isotope composition of marine sulfur may help inform on the causes of ancient environmental and biotic upheavals such as during the Early Triassic (e.g., Payne et al., 2004; Galfetti et al., 2007b; Orchard, 2007; Romano et al., 2013).

Marine barites (Strauss, 1993; Paytan et al., 1998) and evaporites

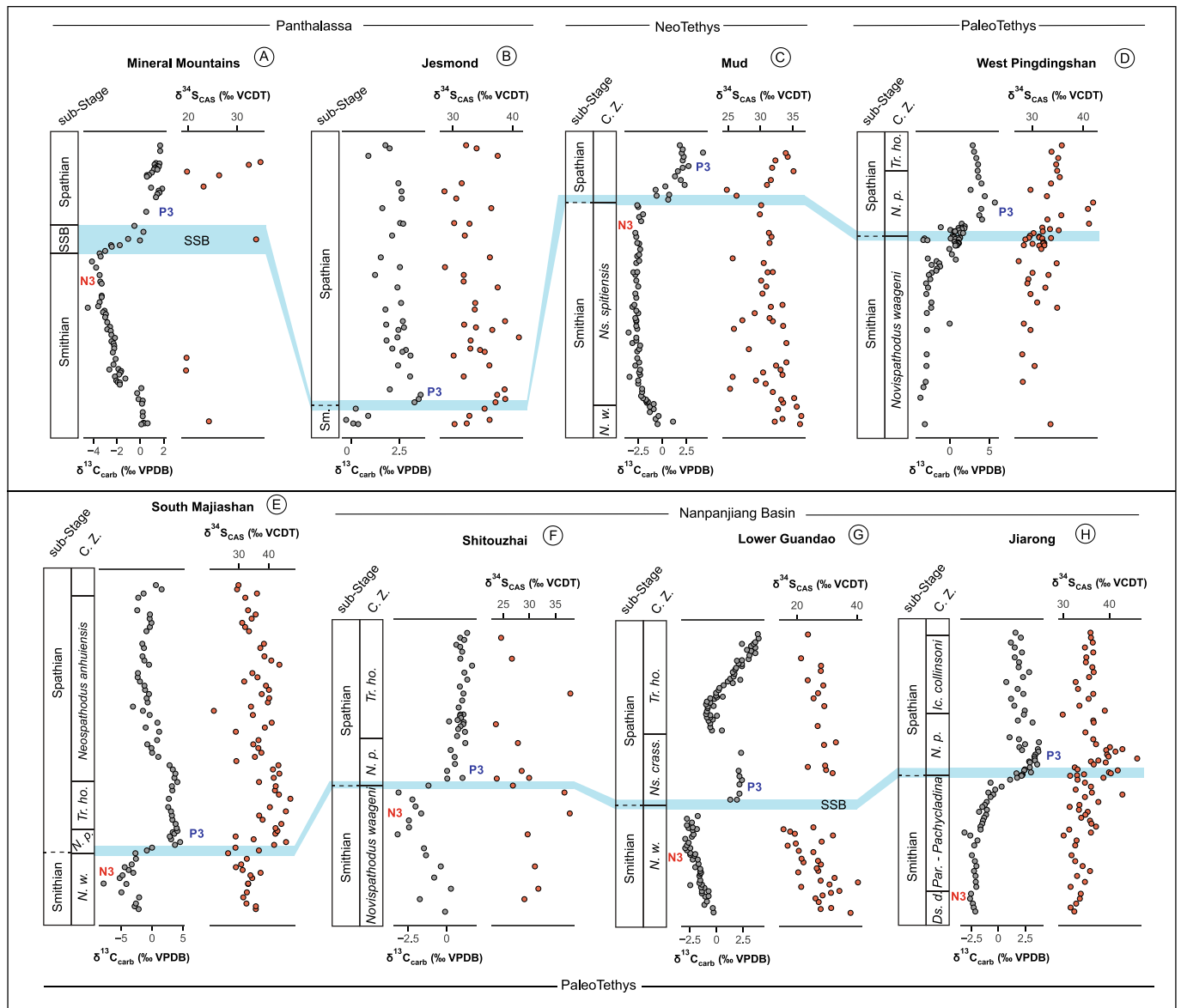


**Fig. 1.** Compilation of published Smithian to Spathian CAS  $\delta^{34}\text{S}$  profiles, as well as  $\delta^{13}\text{C}$  profiles for a) Mineral Mountains section, USA, b) Jesmond section, Canada, c) Mud section, Spiti Valley, India, d) West Pingdingshan section, South China, e) South Majiashan section, South China, f) Shitouzhai section, South China, g) lower Guandao section, South China, and h) Jiarong section, South China. Data sources are as follows: Mineral Mountains – Thomazo et al. (2019), Mud – Stebbins et al. (2019a), West Pingdingshan and Jiarong – Lyu et al. (2019), South Majiashan – Du et al. (2022), Guandao – Song et al. (2014), Shitouzhai – Zhang et al. (2015), Jesmond – Stebbins et al. (2019b). Sm. = Smithian, C.Z. = conodont zone, N.w. = *Novispathodus waageni*, Ns. = *Neospathodus*, N.p. = *Novispathodus pingdingshanensis*, Tr. Ho. = *Triassospathodus homeri*, Ns. Crass. = *Neospathodus crassatus*, Ds. d. = *Discretella discrete*, Par. = *Parachirognathus*, Ic. = *Icriospathodus*.

(Claypool et al., 1980; Cortecci et al., 1981; Strauss, 1997) have been used to reconstruct the marine  $\delta^{34}\text{S}$  evolution through geological time. However, these rocks are rare and do not permit high-resolution studies of variations in the marine  $\delta^{34}\text{S}$  record (Burdett et al., 1989; Hurtgen et al., 2002; Newton et al., 2004). Marine carbonates are, however, much more common as they occur in a wide range of depositional environments. As such, the S-isotope composition of carbonate associated sulfate (CAS) – trace amounts of sulfate which substitutes for carbonate ions in carbonates (Kaplan et al., 1963) – provides a higher resolution  $\delta^{34}\text{S}$  record compared to evaporites and is widely used for investigating the evolution of the marine S cycle (Burdett et al., 1989; Hurtgen et al., 2002). The utility of CAS as a proxy for marine  $\delta^{34}\text{S}$  evolution is based on the understanding that CAS is in isotopic equilibrium with seawater sulfate and that there is almost no isotopic fractionation during the incorporation of sulfate into the calcite crystal lattice (Burdett et al., 1989; Kampschulte et al., 2001; Paris et al., 2014; Barkan et al., 2020). Furthermore, different studies have demonstrated that CAS sulfur is resistant to meteoric and burial diagenesis (e.g., Lyons et al., 2004; Gill et al., 2008; Marenco et al., 2008; Fichtner et al., 2017) and faithfully records seawater S-isotope evolution as recorded by evaporites and barites (Kampschulte and Strauss, 2004; Rennie et al., 2018; Toyama et al., 2020). Nevertheless, this robustness has been challenged by other studies (e.g., Present et al., 2015; Bernasconi et al., 2017; Johnson et al., 2021), which show that compared to evaporites, CAS isotopic data may display considerable scatter/variability within samples and study sites.

The Smithian – Spathian (Olenekian) was a significant interval of the Early Triassic, characterized by notable environmental, climatic, and biotic perturbations. These perturbations are recorded in the biogeochemical cycles of carbon, oxygen, sulfur, mercury, as well as the largest biotic crises for marine nekton during the entire Early Triassic (Payne et al., 2004; Orchard, 2007; Stanley, 2009; Romano et al., 2013; Algeo et al., 2019; Shen et al., 2019; Song et al., 2019; Edward et al., 2024b). Different studies have investigated the evolution of marine  $\delta^{34}\text{S}$  during this interval (Fig. 1; Song et al., 2014; Zhang et al., 2015; Lyu et al., 2019; Song et al., 2019; Stebbins et al., 2019a; Stebbins et al., 2019b; Thomazo et al., 2019; Du et al., 2022), providing insights on climatic and marine paleoenvironmental conditions which potentially impacted the evolution of marine faunas during the Olenekian. Song et al. (2014) suggested that seawater sulfate was depleted in  $^{34}\text{S}$  within the eastern PaleoTethys during the Griesbachian to Smithian, and that Early Triassic marine sulfate variations were probably driven by climate change. Based on a CAS  $\delta^{34}\text{S}$  record from a shallow marine section in South China, Zhang et al. (2015) proposed that oceanic upwelling related to circulation changes due to cooling was responsible for a short-lived marine productivity increase and expansion of “thermocline anoxia” at the Smithian – Spathian boundary (SSB). The notion of climatic cooling and enhanced oceanic overturning circulation driving marine  $\delta^{34}\text{S}$  perturbations across the SSB has been supported by recent studies of marine sections in South China (Lyu et al., 2019; Song et al., 2019), the northern Gondwanan margin (Stebbins et al., 2019a), and mid Panthalassa (Stebbins et al., 2019b). In contrast, Thomazo et al. (2019) ascribed sulfur isotope variations across the late Smithian to early Spathian in the shallow-water marine Mineral Mountains section, USA, to local sedimentological factors. Finally, a recent study (Du et al., 2022) proposed that sulfur and carbon cycle changes recorded during the late Smithian and across the SSB are related to early to middle Smithian volcanic activity.

However, excepting the Jesmond section (Stebbins et al., 2019b), none of the published Smithian – Spathian  $\delta^{34}\text{S}_{\text{CAS}}$  profiles record offshore marine depositional environments, and hence might be influenced by local terrestrial fluxes. Moreover, the Jesmond section only spans the latest Smithian to Spathian (Stebbins et al., 2019b), precluding a comparison of pre-SSB  $\delta^{34}\text{S}_{\text{CAS}}$  trends between offshore carbonate and continental shelf successions. In addition, Early Triassic CAS records display large  $\delta^{34}\text{S}$  variability in individual sections (Fig. 1) and are often offset to higher values relative to contemporaneous evaporites

(Bernasconi et al., 2017), casting doubt on the reliability of CAS for reconstructing Early Triassic marine sulfur cycle variations.

In the current study, variations in the marine sulfur cycle during the Olenekian (middle Smithian to Spathian) and its relation to marine redox and faunal changes are investigated based on CAS extracted from three marine successions deposited in the PaleoTethys and NeoTethys oceans. The studied sections represent deep-water continental shelf (Qiakong section, South China) and shallow- to deep-water offshore (Jebel Aweri and Wadi Musjah sections, Oman) marine environments, respectively (Widmann et al., 2020; Leu et al., 2023). As such, the current study differs from previous studies covering the SSB in that we report CAS isotopic data from both deep-water continental shelf and offshore marine carbonate sections, permitting a more detailed comparison of CAS S-isotope records between these depositional environments during the Olenekian. In addition, the Qiakong section is exceptionally well-constrained by U–Pb zircon absolute ages (Widmann et al., 2020), permitting absolute age-resolved evaluations of the Olenekian marine sulfur cycle. Finally, published Smithian-Spathian CAS  $\delta^{34}\text{S}$  records from around the world are compiled within an absolute age framework and compared with the Olenekian evaporite record (as compiled by Present et al., 2020) to assess global secular marine  $\delta^{34}\text{S}$  trends during the Olenekian.

## 2. Sample Localities

Three marine sections: Qiakong (Nanpanjiang Basin, South China), Wadi Musjah and Jebel Aweri (offshore carbonate build-up blocks deposited in the NeoTethys) were studied (Fig. 2). The Qiakong (QIA) section is situated within the Pingtang syncline, in the northeastern edge of the Nanpanjiang Basin of South China (Fig. 2) (Bagherpour et al., 2020; Leu et al., 2022). This section was deposited in deep-water continental shelf environments and comprises an expanded middle Smithian to Spathian marine sedimentary succession belonging to the Daye and Loulou formations, respectively (Widmann et al., 2020; Leu et al., 2022). The Daye Fm. consists of thin-bedded limestone beds that are considered to represent slope deposits (Widmann et al., 2020). In QIA, the Loulou Fm. contains dark mudstones and black shale units interbedded with thin limestone beds within the late Smithian to basal Spathian (unit IVb). Thereafter, a sharp lithological change (indicative of a hiatus) to thicker nodular limestone units characterizes the rest of the Spathian (Widmann et al., 2020; Leu et al., 2022). Volcanic ash beds are found throughout the Smithian and Spathian units of this succession (Widmann et al., 2020).

The QIA section has been extensively studied in terms of its biostratigraphy, U–Pb zircon geochronology, as well as the carbon isotope and mercury record (Widmann et al., 2020; Leu et al., 2022; Edward et al., 2024b). As such, this section is chronostratigraphically well-constrained via U–Pb zircon absolute ages and conodont unitary association zones (UAZs) (see Widmann et al., 2020 and Leu et al., 2022 for details). The SSB in this section is constrained within the interval of separation between UAZ 7 and UAZ 8 (Leu et al., 2022), with the ash bed within this interval (QIA 7 T) having an absolute age of  $249.292 \pm 0.063$  Ma (Widmann et al., 2020). Further details on the facies description and paleodepositional environment of this section are included in the supplementary information.

The Wadi Musjah (WMJ) section represents a condensed (4.6 m-thick) Hallstatt-type limestone succession deposited in relatively deep water as an isolated oceanic carbonate build-up on seamounts in the NeoTethys ocean during the Early Triassic (Brühwiler et al., 2012; Baud, 2013; Leu et al., 2023). The WMJ section spans the middle Smithian to Spathian based on conodont and ammonoid biochronology and in the present-day, is located about 75 km from Muscat, Oman (Brühwiler et al., 2012; Leu et al., 2023). This section contains conodont- and ammonoid-rich carbonate strata that consist of peloidal grainstone and cemented bivalve coquina biostromes, as well as brachiopod biostromes (Baud et al., 2001). Similarly, the Jebel Aweri (JA) section was

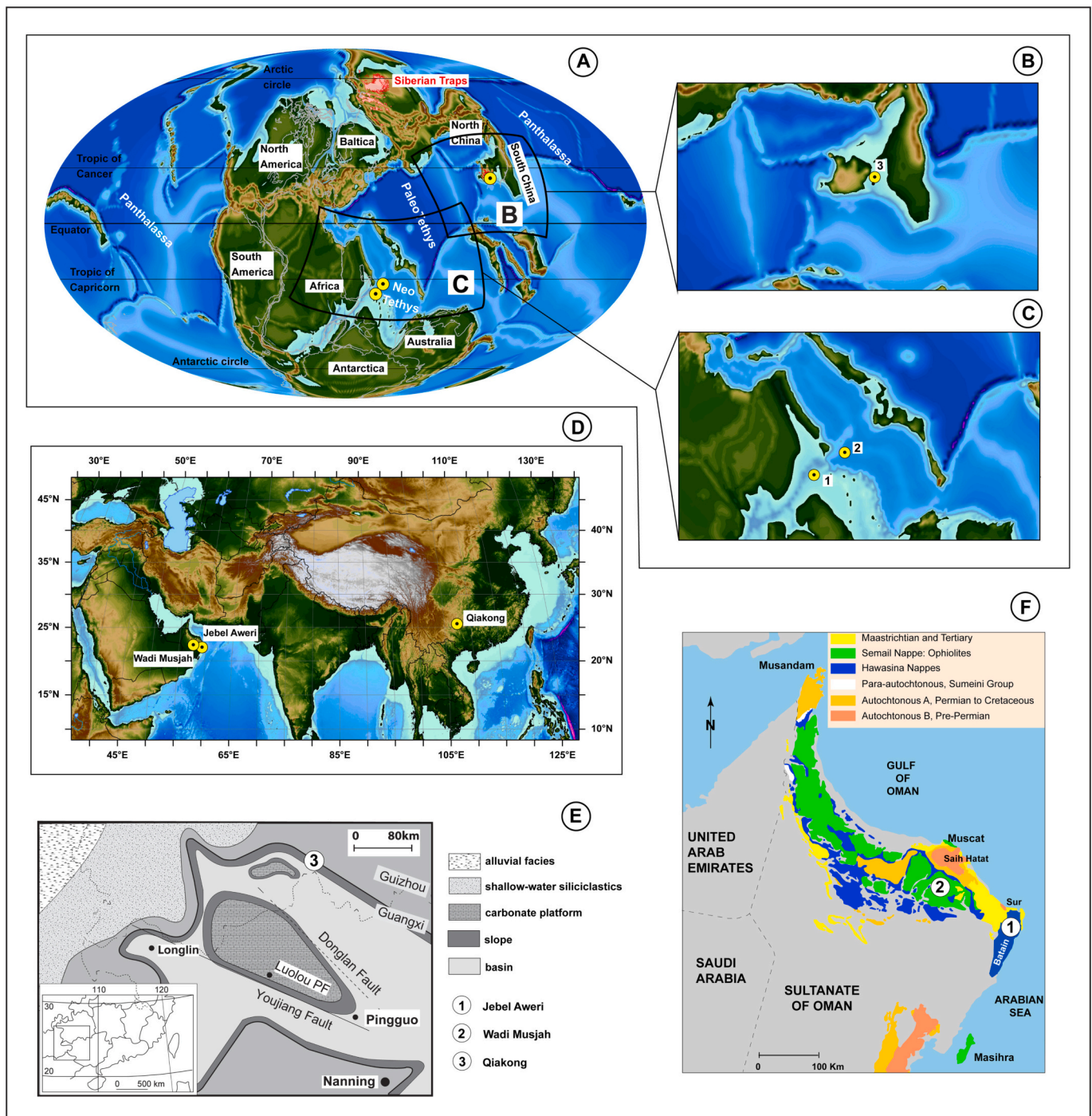


**Fig. 2.** A) Early Triassic paleogeographic map after the Panalasis model (Vérard, 2019), showing the studied successions (yellow circles). Mollweide projection of the B) South China (PaleoTethys) and C) Oman (NeoTethys) areas during the Early Triassic from A. D) Present-day map showing the location of the study sections. Geological map of E) the Nanpanjiang basin after Bagherpour et al. (2017) showing the Qiakong section, and F) Oman with the present-day locations of the offshore carbonate successions, modified after Baud et al. (2001). (For interpretation of the references to colour in this figure legend, the reader is referred to the web version of this article.)

deposited as an exotic build-up block on a seamount within the Neo-Tethys. Today, the JA exotic block is situated within the Batain plains of northeastern Oman (Fig. 2F), having been redeposited as an olistostrome among Middle Jurassic-aged strata of the Guwayza Formation and the Ad Daffah conglomerate (Schreurs and Immenhauser, 1999; Hauser et al., 2001). Unlike WMJ, the JA succession represents an expanded late Smithian to Spathian 30 m-thick sedimentary succession. This exotic block is a shallow water offshore reefal succession containing shell-supported biostrome, cemented lime clasts and microbialite bioherm

(Leu et al., 2023). Both the WMJ and JA successions are temporally well-constrained through conodont and ammonoid biostratigraphy (Brühwiler et al., 2012; Leu et al., 2023). As such, the SSB for both successions is also well-constrained, not only based on an intercalibration of conodont and ammonoid biostratigraphy, but also the carbon isotope record, which situates this boundary within the interval of separation between UAZs 3 and 4 (Leu et al., 2023).

### 3. Methods

Carbon isotope compositions and major and trace element concentrations for the investigated sections were previously analyzed (Leu et al., 2022, 2023; Edward et al., 2024b). For the current study, bulk rock samples from 81 carbonate strata from the three studied sections (QIA = 28, WMJ = 21, JA = 32) were processed for CAS extraction and isotope analyses at the University of Lausanne (UNIL).

#### 3.1. CAS and CRS extraction

CAS extraction was based on the extraction protocol used at UNIL (Bagnoud-Velásquez et al., 2013), which was modified following the recommendations of Wotte et al. (2012). Briefly, 50 to 80 g of powdered samples ( $n = 99$ ) were leached with 10% NaCl solution for at least 8 h to remove NaCl-soluble sulfur. This step was followed by the decantation of the supernatant, after which the leaching step was repeated four times. The samples were then washed with excess Milli-Q water five times to remove any traces of NaCl before dissolution in 37% HCl to release CAS. Samples were acidified at room temperature within 2 h, maintaining the pH of the slurry above 3 to avoid pyrite oxidation, and then filtered through 0.45  $\mu\text{m}$  nitrocellulose filters. The pH of the filtrate was lowered to  $\sim 2$ , followed by heating to 95  $^{\circ}\text{C}$  for 3 h. Subsequently, excess 12% BaCl<sub>2</sub> solution was added, and the solution left to cool and precipitate BaSO<sub>4</sub> at room temperature over three days. The solution containing the precipitated BaSO<sub>4</sub> was filtered over a 0.2  $\mu\text{m}$  nitrocellulose filter to collect the precipitated BaSO<sub>4</sub>, which was then washed with warm Milli-Q water and dried at 50  $^{\circ}\text{C}$  for 24 h. The total amount of recovered BaSO<sub>4</sub> was weighed before isotopic analysis. Further details on the BaSO<sub>4</sub> precipitation process and purification are provided in Spangenberg et al. (2022). CAS concentrations were calculated from the amount of recovered precipitate and its sulfur content determined by EA/IRMS (see supplementary information).

The chromium reducible sulfur (CRS) was extracted from a subset of middle Smithian to Spathian-aged samples which were previously treated for CAS extraction. The solid residue from CAS extraction was washed thoroughly with deionized water until a neutral pH was achieved. Only QIA samples ( $n = 16$ ) were extracted for CRS; JA and WMJ samples, containing generally >99% carbonate, did not yield sufficient solid residue for CRS separation after the acid treatment. The washed residues of QIA samples were dried at 50  $^{\circ}\text{C}$  for >3 days and weighed. CRS (found to be only pyrite) was extracted from 1 to 3 g of the dried residue using a modified chromium reduction method (Canfield et al., 1986). In short, the sample powder was treated with ethanol to disaggregate the powder and then boiled with freshly prepared acidic chromium (II) chloride 1 M solution under a continuous flow of clean nitrogen, releasing H<sub>2</sub>S gas from pyrite. A zinc acetate solution trapped the evolved H<sub>2</sub>S gas as ZnS. The ZnS was converted to Ag<sub>2</sub>S by adding AgNO<sub>3</sub> to the (ZnS-containing) trapping solution and stored at room temperature in the dark for at least 1 day. The Ag<sub>2</sub>S precipitate was filtered through a 0.2  $\mu\text{m}$  nitrocellulose filter, rinsed with 5% ammonia solution and Milli-Q water, and dried at 40  $^{\circ}\text{C}$  for 48 h before isotopic analysis.

#### 3.2. Sulfur and oxygen isotope analyses

Sulfur isotope measurements were performed via elemental analysis-isotope ratio mass spectrometry (EA/IRMS), using a Carlo Erba 1108 elemental analyzer connected to a Thermo Fisher Delta V Plus isotope ratio mass spectrometer following the procedures outlined in Spangenberg et al. (2022). Aliquots of 2–3 mg BaSO<sub>4</sub> (for  $\delta^{34}\text{S}_{\text{CAS}}$ ) or 0.3–0.5 mg Ag<sub>2</sub>S (for  $\delta^{34}\text{S}_{\text{CRS}}$ ) were weighed into tin capsules in duplicates and sealed. Analytical precision for  $\delta^{34}\text{S}_{\text{CAS}}$  was monitored by repeat analyses of international reference materials (IAEA-SO-5, IAEA-SO-6 and NBS 127) and internal standards (Fx-sulfate and UVA-sulfate, with  $\delta^{34}\text{S}_{\text{VCDT}}$  values of  $17.82 \pm 0.22$  ‰ and  $12.73 \pm 0.21$  ‰, respectively

(Spangenberg et al., 2022)). For  $\delta^{34}\text{S}_{\text{CRS}}$ , analytical precision was monitored by replicate measurements of international reference material: IAEA-S3 (silver sulfide), as well as internal standards: UNIL-Cin (cinnabar) and UNIL-PyE (pyrite). Analytical uncertainty was generally 0.30 ‰ or better for  $\delta^{34}\text{S}$  based on repeat analyses of NBS 127.  $\delta^{34}\text{S}_{\text{CAS}}$  and  $\delta^{34}\text{S}_{\text{CRS}}$  values are reported as mean values of replicate analyses ( $\pm 1\sigma$ ) in per mille (‰) notation relative to Vienna-Canyon Diablo Troilite (VCDT).

For CAS  $\delta^{18}\text{O}$  analysis, 0.25–0.3 mg of extracted BaSO<sub>4</sub> was weighed into silver capsules, alongside 0.15 mg of pulverized graphite and sealed. Isotopic compositions were analyzed using a Thermo Scientific FlashSmart CHNS/O Elemental Analyzer coupled to a Thermo Finnigan MAT 253 isotope ratio mass spectrometer at UNIL. The reactor of the Elemental Analyzer was held at a temperature of 1350  $^{\circ}\text{C}$ , and the evolved gas of the samples passed over a gas chromatograph (GC) at 80  $^{\circ}\text{C}$  using a helium flow rate of 100 ml/min. Analytical precision was monitored by replicate measurements of international reference materials: NBS 127 and OGS (barium sulfate), IAEA-601 (benzoic acid), as well as internal standards: SAAS and ANZO (water). Analytical precision was 0.51 ‰ ( $1\sigma$ ) or better based on replicate analysis of IAEA-601. Results are reported as mean values of replicate analyses ( $\pm 1\sigma$ ) in per mille (‰) relative to VSMOW. For samples without replicates, analytical uncertainty is reported using that of the standard material with the highest standard deviation (i.e., IAEA-601: 0.51 ‰).

#### 3.3. Rare earth elements (REE) analysis

Rare earth elements (REE) concentrations of carbonate samples from WMJ ( $n = 23$ ) were measured by quadrupole ICP-MS (Agilent 7700) at the ICP Centre of the University of Geneva. The samples were digested overnight using concentrated HNO<sub>3</sub> in sealed Teflon vials on a hotplate. Instrumental uncertainty was <5% for REE concentrations below 100 ppb. NIST Nd elemental standard was regularly measured at 10 ppb and 100 ppb and yielded relative standard deviation (RSD) of <3%. A mixture of Re and Rh was used as internal standards. REE concentrations were normalized relative to Post Archean Australian Shale (PAAS) (Taylor and McLennan, 1985). The cerium (Ce) and europium (Eu) anomalies (Lawrence et al., 2006; De Baar et al., 1985) were calculated based on the PAAS-normalized values as follows:

$$\text{Ce}_{\text{anom}} = \text{Ce}_N / (Pr_N^2 / Nd_N) \quad (1)$$

$$\text{Eu}_{\text{anom}} = 2 \times \text{Eu}_N / (\text{Sm}_N + \text{Gd}_N) \quad (2)$$

where  $N$  = REE values normalized relative to PAAS.

#### 3.4. Thin section petrography

The textural properties of QIA rock samples were investigated by thin section petrography. Thin sections were prepared from hand samples corresponding to strata investigated for CAS extraction and isotopic analyses at the Paleontological Institute, University of Zurich. Thin section petrography for WMJ and JA strata have been published by Leu et al. (2023).

#### 3.5. Stratigraphic correlation framework

The three studied sections (QIA, WMJ, JA) were correlated using the biostratigraphical correlation framework of Leu et al. (2023), which is based on conodont and ammonoid faunas found in Oman and South China (Fig. 3). Absolute age constraints are based on U–Pb zircon ages for conodont unitary association zone boundaries in the QIA section, which is the most expanded U–Pb zircon dated Smithian – Spathian section so far (Widmann et al., 2020). Note that the conodont UAZ numbering for QIA by Widmann et al. (2020) has been updated by Leu et al. (2022), and that the latter UAZ numbering is applied herein.



Smithian and Spathian, were used to further refine the stratigraphic correlation between QIA, WMJ and JA, as well as correlations to other sections in the literature. To ensure consistency in the delineation of the SSB between the current study and previously published CAS  $\delta^{34}\text{S}$  records (Fig. 1), the midpoint of the transition from the N3 to P3 CIE was used to correlate the SSB (as suggested by Zhang et al. (2019b)). However, it should be noted that the P3 peak is usually associated with a hiatus of variable duration (Widmann et al., 2020). The SSB was assigned the absolute age of 249.29 Ma after Widmann et al. (2020) and the N3 minimum was assigned the absolute age of 250.038 Ma based on its correlation to the base of UAZ 5 in QIA (Fig. 4). Based on the tie-points and the reported stratigraphic heights in the relevant literature, LSRs, A<sub>0</sub> and A<sub>1</sub> were calculated for each section, as well as linearly interpolated ages for samples between each tie-point.

## 4. Results

The CAS concentration and isotopic data ( $\delta^{34}\text{S}_{\text{CAS}}$ ,  $\delta^{34}\text{S}_{\text{CRS}}$ , and  $\delta^{18}\text{O}_{\text{CAS}}$ ), as well as REE data generated for this study are presented in the supplementary data file (Edward et al., 2024a) and visualized in Figs. 4 to 6.

### 4.1. Sulfur isotopes

The exceptional age control available for the studied sections (Widmann et al., 2020; Leu et al., 2022; Leu et al., 2023) enables the current CAS  $\delta^{34}\text{S}$  results to be evaluated within a precise chronostratigraphic framework.  $\delta^{34}\text{S}_{\text{CAS}}$  values within the studied interval have a wide range for QIA (21–39 ‰) relative to WMJ (22–28 ‰) and JA (24–31 ‰). CAS  $\delta^{34}\text{S}$  within the middle to upper Smithian of QIA show

an overall decreasing trend. However, a positive excursion is recorded across the SSB (Fig. 4). This positive  $\delta^{34}\text{S}_{\text{CAS}}$  excursion is also observed in  $\delta^{34}\text{S}_{\text{CRS}}$  and coincides with the globally recorded P3 positive CIE (Song et al., 2013). Difference in the  $\delta^{34}\text{S}$  values of co-occurring CAS and CRS ( $\Delta^{34}\text{S}_{\text{CAS-CRS}}$ ), assumed to be pyrite, has a range between 25 and 54 ‰.  $\Delta^{34}\text{S}_{\text{CAS-CRS}}$  values increase in tandem with  $\delta^{34}\text{S}_{\text{CAS}}$  across the SSB (Fig. 4f) and have a positive correlation with  $\delta^{34}\text{S}_{\text{CAS}}$  (Spearman's  $r = 0.76$ ,  $p = 0.00$ ), suggesting that  $\Delta^{34}\text{S}_{\text{CAS-CRS}}$  variation is mainly driven by  $\delta^{34}\text{S}_{\text{CAS}}$ .

For JA, which has the most expanded late Smithian record (~20 m) and no apparent SSB unconformity (Leu et al., 2023), a gradual change of about +7 ‰ for  $\delta^{34}\text{S}_{\text{CAS}}$  is recorded within the entire late Smithian (UAZ 1 to UAZ 3; Fig. 5). Here, maximum values (ca. 31 ‰) are recorded within the SSB interval of separation (Fig. 5). This late Smithian to SSB positive trend is succeeded by a 3 ‰ decrease in the basal Spathian (UAZ 4 to base of UAZ 5). Thereafter,  $\delta^{34}\text{S}_{\text{CAS}}$  values remain around 27 ‰ for the rest of the JA Spathian record. The WMJ section records a gradual overall 6 ‰ increase in  $\delta^{34}\text{S}_{\text{CAS}}$  values across the middle Smithian to SSB, also reaching maximum values within the SSB interval of separation (Fig. 6). This increasing trend is interrupted by a ca. 4 ‰  $\delta^{34}\text{S}_{\text{CAS}}$  decline at the basal Spathian (i.e., within UAZ 4). Afterwards, a return to SSB  $\delta^{34}\text{S}_{\text{CAS}}$  values of ca. 27 ‰ is recorded before a final decline to lower values (ca. 22 ‰) at the top of UAZ 7.

### 4.2. Oxygen isotopes

For QIA, CAS  $\delta^{18}\text{O}$  values have a range between 11 and 20 ‰, whereas JA and WMJ have a range between 14 and 25 ‰ and 12–26 ‰, respectively. CAS  $\delta^{18}\text{O}$  values prior to the SSB for QIA (Fig. 4d) are relatively constant between 15 and 17 ‰ (except sample Q133 with

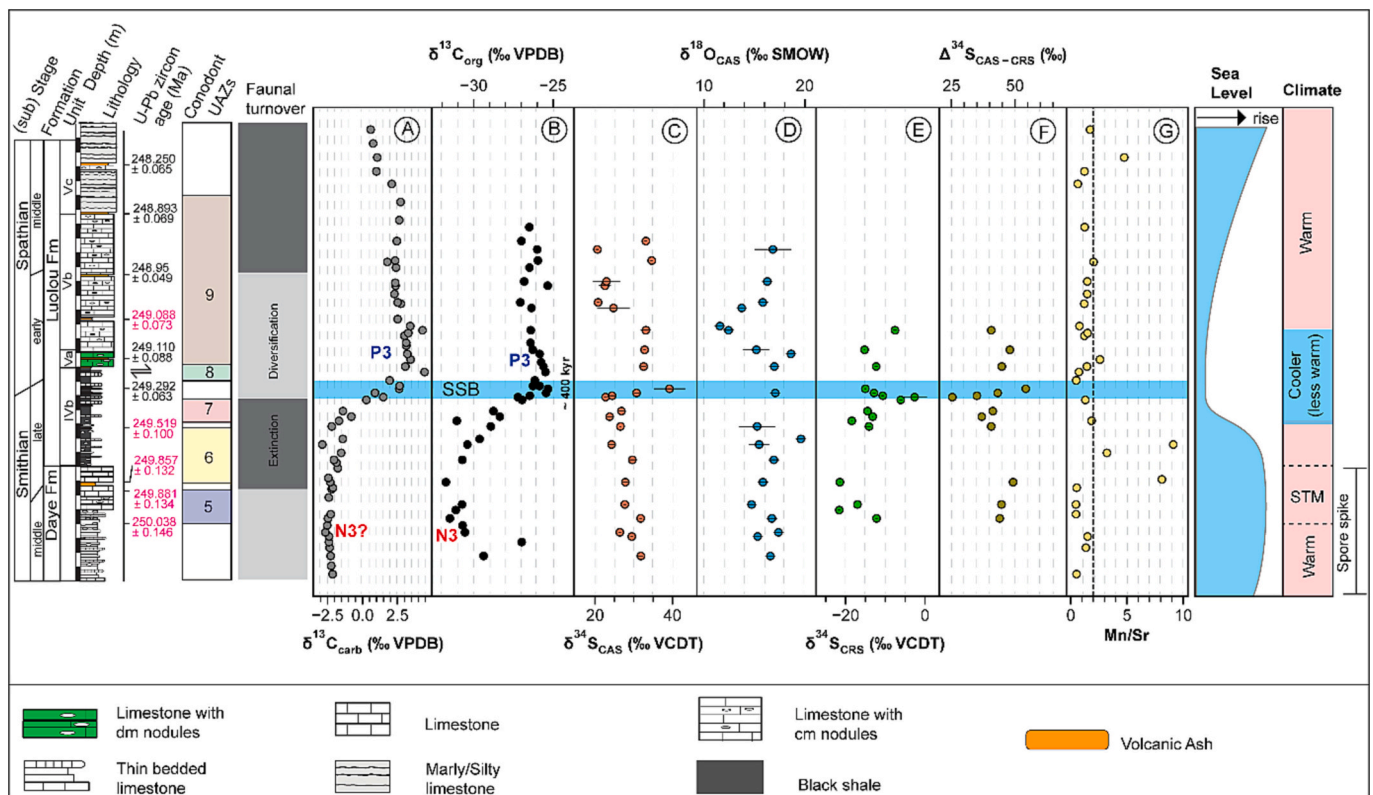


**Fig. 4.** Geochemical profile showing the A)  $\delta^{13}\text{C}_{\text{carb}}$ , B)  $\delta^{13}\text{C}_{\text{org}}$ , C)  $\delta^{34}\text{S}_{\text{CAS}}$ , D)  $\delta^{18}\text{O}_{\text{CAS}}$ , E)  $\delta^{34}\text{S}_{\text{CRS}}$ , F)  $\Delta^{34}\text{S}_{\text{CAS-CRS}}$ , G) Mn/Sr profiles for the Qiakong section. UAZ = unitary association zone. Lithostratigraphic log, U–Pb zircon ages and  $\delta^{13}\text{C}_{\text{carb}}$  values are from Widmann et al. (2020). The ages denoted in pink represent those interpolated by Bayesian age-depth modeling (Widmann et al., 2020).  $\delta^{13}\text{C}_{\text{org}}$  values and Mn, and Sr values are from Edward et al. (2024b). Conodont UAZs and faunal turnover (based on conodonts) are from Leu et al. (2022). Climate depiction and timing is after Goudebrand et al. (2019) and Widmann et al. (2020). The spore spike interval is after Hermann et al. (2011). Relative sea level changes depiction is after Zhang et al. (2015). STM = Smithian thermal maximum. (For interpretation of the references to colour in this figure legend, the reader is referred to the web version of this article.)

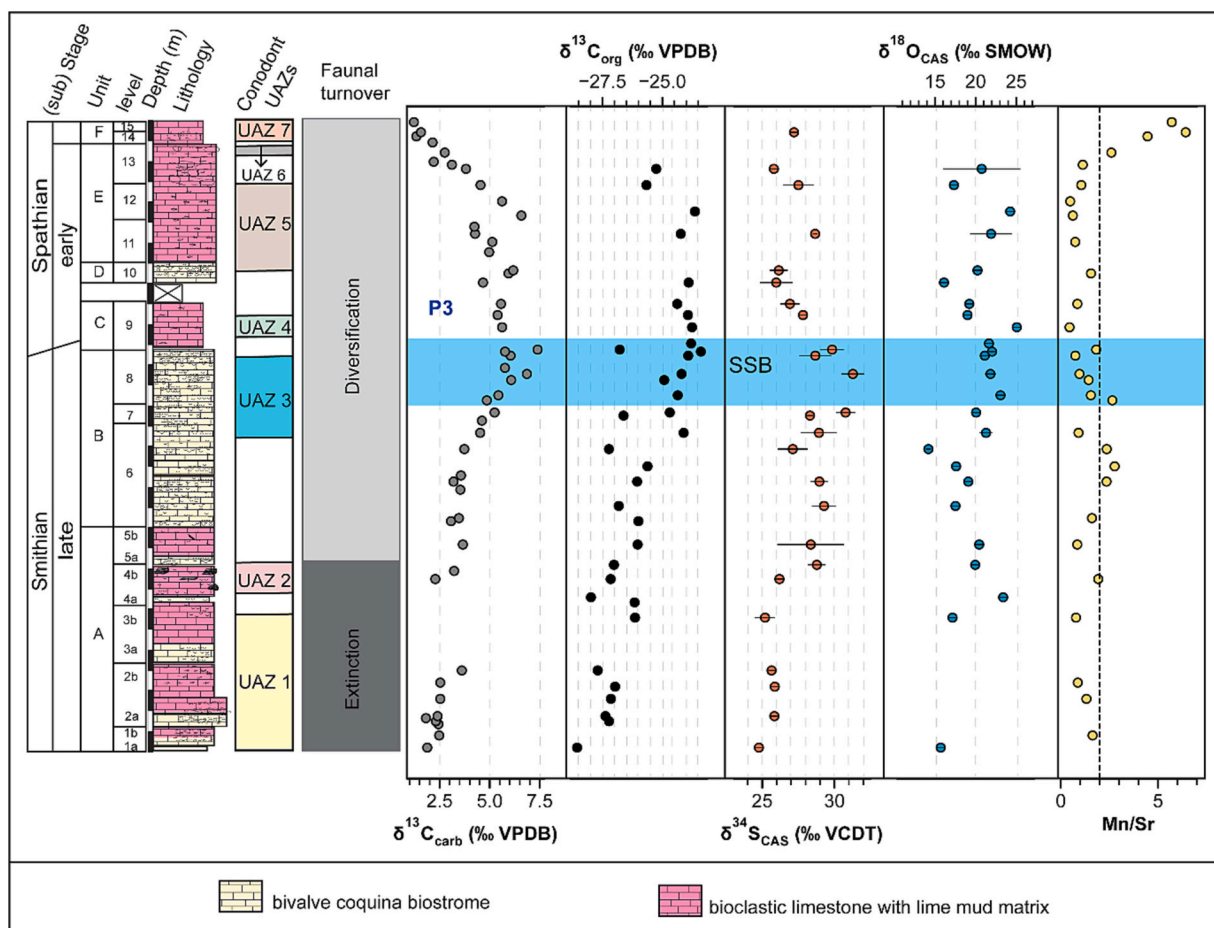


**Fig. 5.** Geochemical profiles of the Jebel Awari section showing the  $\delta^{13}\text{C}_{\text{carb}}$ ,  $\delta^{13}\text{C}_{\text{org}}$ ,  $\delta^{34}\text{S}_{\text{CAS}}$ ,  $\delta^{18}\text{O}_{\text{CAS}}$  and Mn/Sr record for the late Smithian to Spathian interval. The SSB is defined as the interval of separation between UAZs 3 and 4 (Leu et al., 2023).  $\delta^{13}\text{C}_{\text{carb}}$  and conodont faunal turnover data are from Leu et al. (2023). Mn/Sr and  $^{87}\text{Sr}/^{86}\text{Sr}$  data are from Edward et al. (2024b). The vertical black dashed line depicts the Mn/Sr preservation limit applied (2).

$\delta^{18}\text{O}$  value of ca. 20 ‰) and display an increasing trend across the SSB. Subsequently, a decrease in values by 4 ‰ is recorded in the early Spathian (Fig. 4d), followed by a recovery to background values of about 16 ‰ as noted prior to the SSB. Both WMJ and JA display an overall  $\delta^{18}\text{O}_{\text{CAS}}$  increase during the Smithian towards the SSB similar to the  $\delta^{34}\text{S}_{\text{CAS}}$  record. Also, both sections show a general decrease in  $\delta^{18}\text{O}$  in the early Spathian, similar to the decrease in  $\delta^{18}\text{O}_{\text{CAS}}$  values for QIA, albeit somewhat further above the SSB.

#### 4.3. CAS concentrations

CAS concentrations were stoichiometrically calculated from the amount of recovered precipitate following CAS extraction. The calculated CAS content was then normalized to total sulfur (TS) content determined by EA/IRMS (e.g., Witts et al., 2018), as pure barite has 13.74 wt% S. The TS content of recovered CAS-BaSO<sub>4</sub> was on average 8.83 wt%, indicating that not all recovered precipitate was indeed barite. We tentatively attribute this discrepancy between expected and measured TS content to BaCl<sub>2</sub> reprecipitation due to the excess 12% BaCl<sub>2</sub> solution used for CAS extraction. However, this requires further study. Calculated CAS concentrations for QIA, JA and WMJ have a range between 85 and 423 ppm, 2 and 2283 ppm, and 2 and 2089 ppm, respectively. These CAS contents show no correlation to either CAS  $\delta^{34}\text{S}$  or  $\delta^{18}\text{O}$  (Fig. 7, Fig. S15), suggesting that CAS concentrations have no measurable influence on CAS isotopic compositions in the present study.

#### 4.4. REE concentrations

Analyzed samples have a REE pattern consistent with that of modern seawater, displaying a prominent negative Ce anomaly (Fig. 8A), and a mean  $\text{Eu}_{\text{anom}}$  value of 1.01 (German and Elderfield, 1990; Alibo and Nozaki, 1999). Total REE concentrations are between 0.2 and 5.8 ppm, except for sample WMJ 17C (303.4 ppm) and are generally lower in the Smithian relative to the Spathian.  $\text{Ce}_{\text{anom}}$  values have a range between 0.21 and 1.09 ppm, with the Smithian being characterized by higher values (between 0.7 and 1 ppm) relative to the Spathian (< 0.7 ppm).

## 5. Discussion

### 5.1. Assessing the preservation of primary CAS isotopic information

Primary marine CAS  $\delta^{34}\text{S}$  and  $\delta^{18}\text{O}$  values have the potential to be altered by post-depositional diagenetic processes (e.g., increasing sedimentary burial, dolomitization, carbonate dissolution and recrystallization in diagenetic pore fluids) or sample contamination during laboratory CAS extraction (Marenco et al., 2008; Wotte et al., 2012; Present et al., 2015; Fichtner et al., 2017). Different techniques are commonly applied in assessing the preservation of primary CAS compositions. These include the evaluation of Mn/Sr ratios and cross-plots of CAS isotope and geochemical data (e.g., Hurtgen et al., 2002; Gill et al., 2008; Marenco et al., 2008; Johnson et al., 2021; Du et al., 2022; Kwon et al., 2022), as well as statistical smoothing of CAS isotope curves to elucidate overall trends and attenuate the impact of outliers (e.g.,

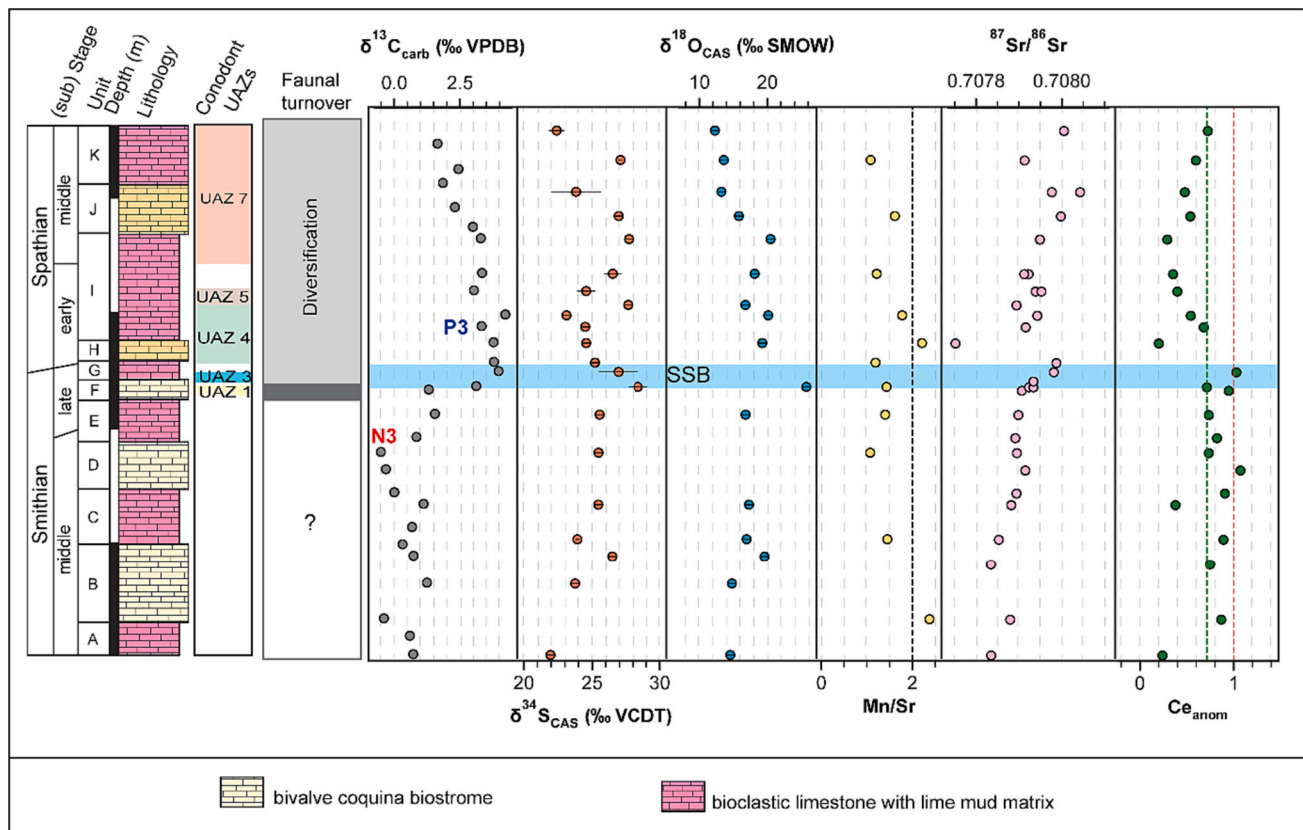


**Fig. 6.** Geochemical profiles of the Wadi Musjah (WMJ) section showing the  $\delta^{13}\text{C}_{\text{carb}}$ ,  $\delta^{34}\text{S}_{\text{CAS}}$ ,  $\delta^{18}\text{O}_{\text{CAS}}$ , Mn/Sr,  $^{87}\text{Sr}/^{86}\text{Sr}$  and Cerium anomaly ( $\text{Ce}_{\text{anom}}$ ) record for the middle Smithian to Spathian interval. The Smithian – Spathian boundary is defined after [Leu et al. \(2023\)](#).  $\delta^{13}\text{C}_{\text{carb}}$  and conodont faunal turnover data are from [Leu et al. \(2023\)](#). Mn/Sr and  $^{87}\text{Sr}/^{86}\text{Sr}$  data are from [Edward et al. \(2024b\)](#). The vertical dashed red line depicts the typical Ce anomaly value ( $\text{Ce}_{\text{anom}}$ ) for anoxic seawater (i.e., 1, [Liu et al., 2021](#)), the red dashed line depicts the median  $\text{Ce}_{\text{anom}}$  value (0.71), and the black dashed line depicts the Mn/Sr preservation limit applied. (For interpretation of the references to colour in this figure legend, the reader is referred to the web version of this article.)

[Kampschulte and Strauss, 2004](#); [Song et al., 2014](#)). Furthermore, significant heterogeneity of  $\delta^{34}\text{S}_{\text{CAS}}$  values ( $> 5\%$ ) within individual bulk carbonate samples may result from diagenetic alteration and/or the mixing of CAS from different carbonate components such as micrite, skeletal fragments and calcite cements ([Present et al., 2015](#); [Johnson et al., 2021](#)). In addition, diagenetic modification of CAS  $\delta^{34}\text{S}$  may be expressed by an inverse relationship between CAS concentrations and  $\delta^{34}\text{S}$  values ([Johnson et al., 2021](#)).

Mn/Sr ratios for most strata in the present study are  $< 2$  and have no correlation to  $\delta^{34}\text{S}_{\text{CAS}}$  values ([Fig. 7c, e](#)). Also, Mg/Ca ratios are  $< 0.1$  and have no correlation to  $\delta^{34}\text{S}_{\text{CAS}}$  nor  $\delta^{18}\text{O}_{\text{CAS}}$ , and no correlation is observed between CAS concentrations (depicted as  $1/[\text{CAS}]$ ) and  $\delta^{34}\text{S}_{\text{CAS}}$  ([Fig. 7c](#)). Furthermore,  $\delta^{34}\text{S}$  and  $\delta^{18}\text{O}$  values determined by multiple analyses of individual samples are similar, mostly varying by  $< 4\%$ . However, three samples: Q146, Q148, and JA 34C show differences as large as  $7.2\%$  (for  $\delta^{18}\text{O}_{\text{CAS}}$ ) and  $9.5\%$  (for  $\delta^{34}\text{S}_{\text{CAS}}$ ), suggesting that non-primary CAS isotopic values are also recorded by these samples.

Although of very limited stratigraphic resolution, existing evaporite data indicate that the Olenekian was characterized by  $\delta^{34}\text{S}$  values between 24 and 32 ‰, although lower values of ca. 17 ‰ are recorded at the Olenekian – Anisian boundary ([Claypool et al., 1980](#); [Cortecci et al., 1981](#); [Insalaco et al., 2006](#); [Marenco et al., 2008](#); [Horacek et al., 2010](#); [Bernasconi et al., 2017](#)). The main Smithian – Spathian range of evaporite  $\delta^{34}\text{S}$  values (24–32 ‰) is similar to  $\delta^{34}\text{S}_{\text{CAS}}$  values recorded for JA (24–31 ‰) and WMJ (22–28 ‰) ([Figs. 5–6](#)), suggesting that these two sections preserve near-primary Olenekian seawater  $\delta^{34}\text{S}$  values. Furthermore, the WMJ section displays REE characteristics similar to that of modern seawater ([Fig. 8A](#); [Section 4.4](#)) and the Sr isotope records

of WMJ and JA are consistent with the global Sr isotope trend and absolute values for the Early Triassic ([Edward et al., 2024b](#)). In addition, WMJ and JA strata mostly consist of biogenic calcite components ([Fig. 9](#)), a carbonate phase known to reliably record seawater S-isotope compositions ([Kampschulte and Strauss, 2004](#)). These considerations strongly support the inference that the Oman offshore sections preserve near-primary seawater geochemical information.

In contrast, QIA samples have a wider range of absolute  $\delta^{34}\text{S}$  values (21–39 ‰) relative to the evaporite record, suggesting that  $\delta^{34}\text{S}$  trends recorded for this section may not all be near-primary. Also, thin section photos indicate that unlike WMJ and JA, QIA samples have a low biogenic calcite component and instead are occasionally composed of a combination of carbonate and clastic material ([Fig. 9D](#), supplementary information). Also, partial dissolution of the carbonate and replacement with clastic material or sparry calcite is evident in many QIA samples (see facies description in the supplementary information). Hence, QIA samples are likely to incorporate sulfate from both seawater and terrestrial sources, consistent with the wider range of CAS  $\delta^{34}\text{S}$  values for this section.

## 5.2. Comparison of global Olenekian CAS $\delta^{34}\text{S}$ records

A compilation of previously published CAS  $\delta^{34}\text{S}$  records spanning the Smithian – Spathian enables an assessment of the general CAS  $\delta^{34}\text{S}$  trend during the Olenekian ([Fig. 10](#)). The compiled data indicates that Olenekian CAS  $\delta^{34}\text{S}$  values have a wide range (i.e., between 15 and 47 ‰; [Fig. 8B](#); [Fig. 10A](#)), which is a factor of 4 higher than that of the relatively sparse evaporite record (24–32 ‰; [Present et al., 2020](#) and references therein). Offset between evaporite and CAS  $\delta^{34}\text{S}$  values have previously

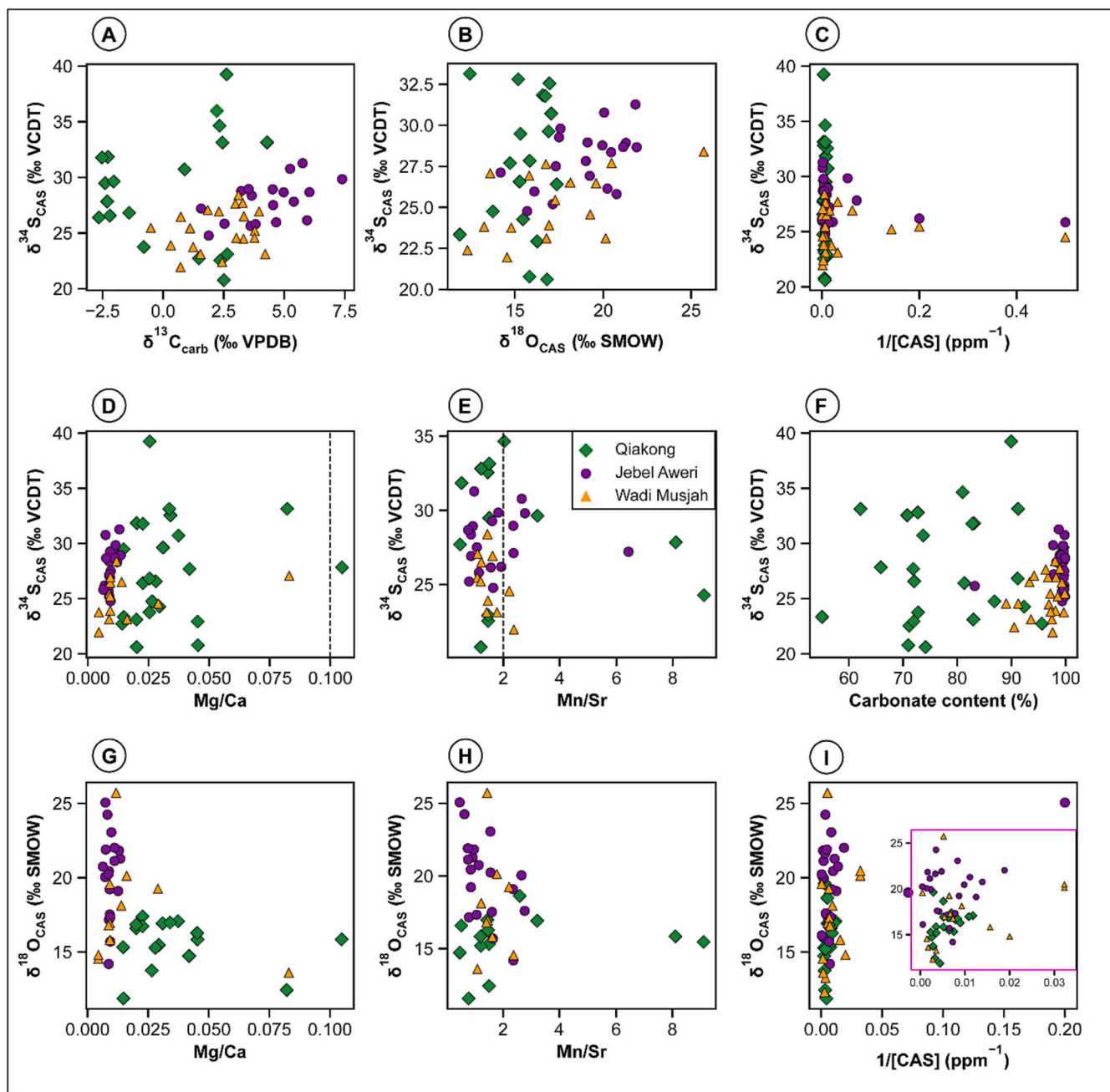


**Fig. 7.** Cross-plots of  $\delta^{34}\text{S}_{\text{CAS}}$  vs A)  $\delta^{13}\text{C}_{\text{carb}}$ , B)  $\delta^{18}\text{O}_{\text{CAS}}$ , C) inverse of CAS concentration ( $1/[\text{CAS}]$ ), D) Mg/Ca ratio, E) Mn/Sr ratio, F) carbonate content, for samples for Qiakong, Jebel Aweri and Wadi Musjah. Cross plots of  $\delta^{18}\text{O}_{\text{CAS}}$  vs G) Mg/Ca, H) Mn/Sr, I)  $1/[\text{CAS}]$ . Inset in pink rectangle plots  $\delta^{18}\text{O}_{\text{CAS}}$  vs  $1/[\text{CAS}]$  excluding the 2 Jebel Aweri samples with the highest  $1/[\text{CAS}]$  values. Mg, Ca, Mn and Sr data are from Edward et al. (2024b). (For interpretation of the references to colour in this figure legend, the reader is referred to the web version of this article.)

been reported for the late Changhsingian to Induan (Permian – Triassic transition), as well as other intervals of the Phanerozoic (Bernasconi et al., 2017; Present et al., 2020; Johnson et al., 2021). The offset between these two archives, as well as observed  $\delta^{34}\text{S}$  variability between coeval CAS samples (Fig. 8B) have been attributed to post-depositional alteration and/or an effect of different constituents (e.g., micrite, skeletal allochems, cements) of individual carbonate samples having different  $\delta^{34}\text{S}$  values (Marenco et al., 2008; Present et al., 2015, 2020; Bernasconi et al., 2017). Considering thin section petrography observations from QIA samples (Fig. 9D) and the discordance between CAS  $\delta^{34}\text{S}$  values for QIA relative to the offshore WMJ and JA successions, we endorse this interpretation.

Nevertheless, a spatially consistent  $\delta^{34}\text{S}$  trend discernible from the

Olenekian CAS record upon (i) comparison of  $\delta^{34}\text{S}$  records from individual sections (Fig. 1) or (ii) fitting a locally weighted scatter plot smoothing (LOWESS) model to the compiled CAS data (Fig. 10A) is that  $\delta^{34}\text{S}$  values increase across the middle Smithian to SSB, followed by a gradual decrease during the Spathian. Also, a positive correlation between carbonate  $\delta^{13}\text{C}$  and CAS  $\delta^{34}\text{S}$  trends between the Smithian and early Spathian interval is observable. Hence, the increase in  $\delta^{34}\text{S}_{\text{CAS}}$  values across the Smithian – Spathian transition is considered a primary global  $\delta^{34}\text{S}$  trend during the Olenekian. Notably, this pattern is consistent with the sparse Olenekian evaporite record, which seems to indicate an increase in  $\delta^{34}\text{S}$  between the middle and late Smithian followed by a Spathian decline towards the Anisian (Fig. 10B; see also Fig. 5 of Bernasconi et al., 2017). Furthermore, an increasing trend in Early Triassic

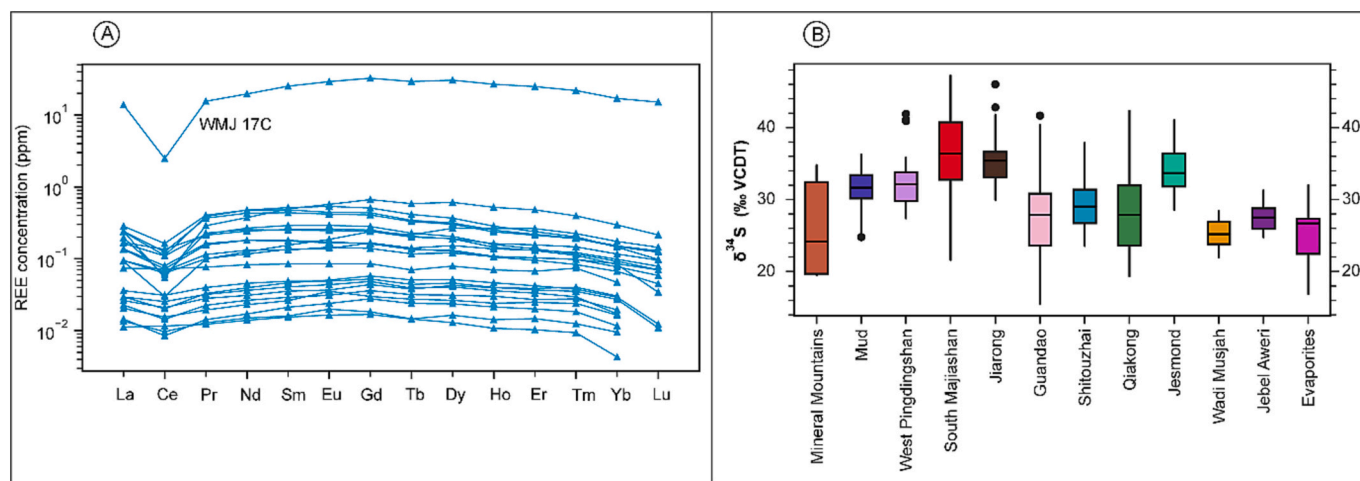


**Fig. 8.** A) Post Archean Australian Shale (PAAS)-normalized spider diagram comparing the rare earth element concentrations for Olenekian carbonate samples from Wadi Musjah (WMJ). PAAS values are from Taylor and McLennan (1985). B) Box plots showing the distribution of CAS  $\delta^{34}\text{S}$  values for Olenekian bulk carbonates and evaporites. Data sources are the same as for Fig. 1 and evaporite data is from the  $\delta^{34}\text{S}$  compilation of Present et al. (2020).

evaporite  $\delta^{34}\text{S}$  was previously documented by earlier workers, although with lower resolution age calibration (e.g., Holser, 1977; Claypool et al., 1980; Holser et al., 1988). Consequently, it is proposed that although some Olenekian CAS  $\delta^{34}\text{S}$  values may have been altered by late diagenetic processes, primary global trends in seawater  $\delta^{34}\text{S}$  evolution over the Olenekian are still preserved by this archive. Our JA and WMJ  $\delta^{34}\text{S}_{\text{CAS}}$  records are overall consistent with the inferred global trend for the Olenekian (Fig. 5, Fig. 6). Similarly, the QIA section records a trend of increasing  $\delta^{34}\text{S}_{\text{CAS}}$  values across the SSB.

### 5.3. Interpretation of the Olenekian CAS isotope records

Given the long residence time of seawater sulfate in the modern oceans, i.e., 13–20 Myr (Claypool et al., 1980; Walker, 1986), primary changes in seawater S-isotope compositions can be expected to only be observable within this temporal resolution. However, very rapid changes (< 10 Myr) in seawater  $\delta^{34}\text{S}$  have been documented for different intervals of geologic time including the Devonian and Early Triassic (e.g., Holser, 1977; Claypool et al., 1980; Kampschulte and Strauss, 2004). As such, it has been suggested (e.g., Bottrell and Newton, 2006) that the oceanic residence time of sulfate was shorter in the geologic past. This suggestion is supported by different evaporite fluid inclusion studies (e.g., Horita et al., 2002; Lowenstein et al., 2003), which indicate that ancient oceans had lower sulfate concentrations than is the case for modern oceans.

Changes towards lower marine  $\delta^{34}\text{S}_{\text{CAS}}$  values can be explained by increased inputs of sulfide-derived sulfur from weathering of continental sediments (typically  $\delta^{34}\text{S}$  values of 0 to 10 ‰; Paytan et al., 1998) and/or of magmatic rocks or even direct volcanic sulfur inputs ( $\delta^{34}\text{S}$  values: 0 to 3.5 ‰; Paytan et al., 1998). In addition, upwelling and oxidation of  $\text{H}_2\text{S}$ -rich bottom waters have been invoked to explain decreasing  $\delta^{34}\text{S}_{\text{CAS}}$  trends (e.g., Zhang et al., 2015; Song et al., 2019). Alternatively, a decrease in the burial of reduced sulfur species in sediments or decreasing MSR rates may account for a trend towards lower  $\delta^{34}\text{S}_{\text{CAS}}$  values (Bottrell and Newton, 2006; Halevy et al., 2012; Schobben et al., 2016). Primary CAS isotopic compositions can be altered via the reoxidation of reduced sulfate produced by MSR during early diagenesis, as well as the mixing of different CAS phases in an individual sample (Bottrell and Newton, 2006; Johnson et al., 2021).

The short-term  $\delta^{34}\text{S}$  variability recorded for QIA prior to and after the SSB (Fig. 4), at odds with the global increasing CAS  $\delta^{34}\text{S}$  trend (Fig. 10), may be explained by post-depositional incorporation of terrestrial sulfide-derived sulfur or the reoxidation of reduced sulfur species during early or late diagenesis. Inferred alteration of primary

seawater CAS S-isotope compositions by the incorporation of terrestrial reduced sulfur species during diagenesis is also compatible with the nearshore continental shelf paleo-depositional environment of the QIA succession (Widmann et al., 2020; Leu et al., 2022) as well as enhanced continental weathering fluxes during the Olenekian (Sedlacek et al., 2014; Edward et al., 2024b). Previous studies indicate that the SSB in the Paleotethys was associated with a ca. 10 ‰ CAS  $\delta^{34}\text{S}$  increase over 500–600 kyr (Lyu et al., 2019; Stebbins et al., 2019b; Du et al., 2022). However, the SSB of the QIA succession is characterized by a rapid increase in  $\delta^{34}\text{S}$  values of 17 ‰ within ca. 55 kyr if the most extreme values around the SSB are considered (i.e., Q136C: 22.70 ‰, Q51: 24.40 ‰ and Q53: 39.25 ‰). Although consistent with an overall increase in  $\delta^{34}\text{S}$  across the Smithian – Spathian transition, the magnitude and speed of the QIA  $\delta^{34}\text{S}$  increase is very unlikely to represent a primary seawater  $\delta^{34}\text{S}$  change. However, if the extreme  $\delta^{34}\text{S}$  values at the SSB are not considered, an increase in  $\delta^{34}\text{S}$  values is still recorded (i.e., 9 ‰ increase within ~400 kyr) which is more consistent with CAS records from other Tethyan localities. Nevertheless, the wide  $\delta^{34}\text{S}$  range of the QIA succession (up to 20 ‰), as well as the rapid short-term changes in the CAS record of this section point to a significant influence of diagenetic processes on this CAS record. As such, the QIA section may be unsuitable for reliable interpretations of global  $\delta^{34}\text{S}$  changes during the studied interval.

In contrast with the QIA section, the WMJ and JA  $\delta^{34}\text{S}_{\text{CAS}}$  records, considered together, indicate a trend of increasing marine  $\delta^{34}\text{S}_{\text{CAS}}$  values from the middle Smithian to SSB (Fig. 5, Fig. 6, Fig. S14B), consistent with the inferred global trend (Fig. 10). The middle Smithian to SSB  $\delta^{34}\text{S}_{\text{CAS}}$  increasing trend can be explained by a decrease in continental weathering of sulfides, or by globally increased rates of net MSR and pyrite burial in Olenekian oceans (e.g., Stebbins et al., 2019a). Considering that the middle to early late Smithian was characterized by a warm climate regime (Hermann et al., 2011; Goudeband et al., 2019), elevated continental weathering fluxes (Sedlacek et al., 2014) and hence, an increase in nutrient and organic carbon delivery to the oceans (Widmann et al., 2020), the preferred interpretation for the middle Smithian to SSB  $\delta^{34}\text{S}_{\text{CAS}}$  trend is an increase in net marine MSR. Increased marine productivity over this interval likely facilitated dissolved oxygen depletion in the water column and increase in MSR. This inference is consistent with the Ce anomaly record for WMJ (Fig. 6), which shows that relative to the Spathian, the Smithian is characterized by higher  $\text{Ce}_{\text{anom}}$  values (i.e., close to 1), indicative of a poorly oxygenated water column (Liu et al., 2021). In addition, the inference of low dissolved oxygen in Smithian oceans is consistent with previous suggestions of expanded middle to late Smithian oceanic anoxia based

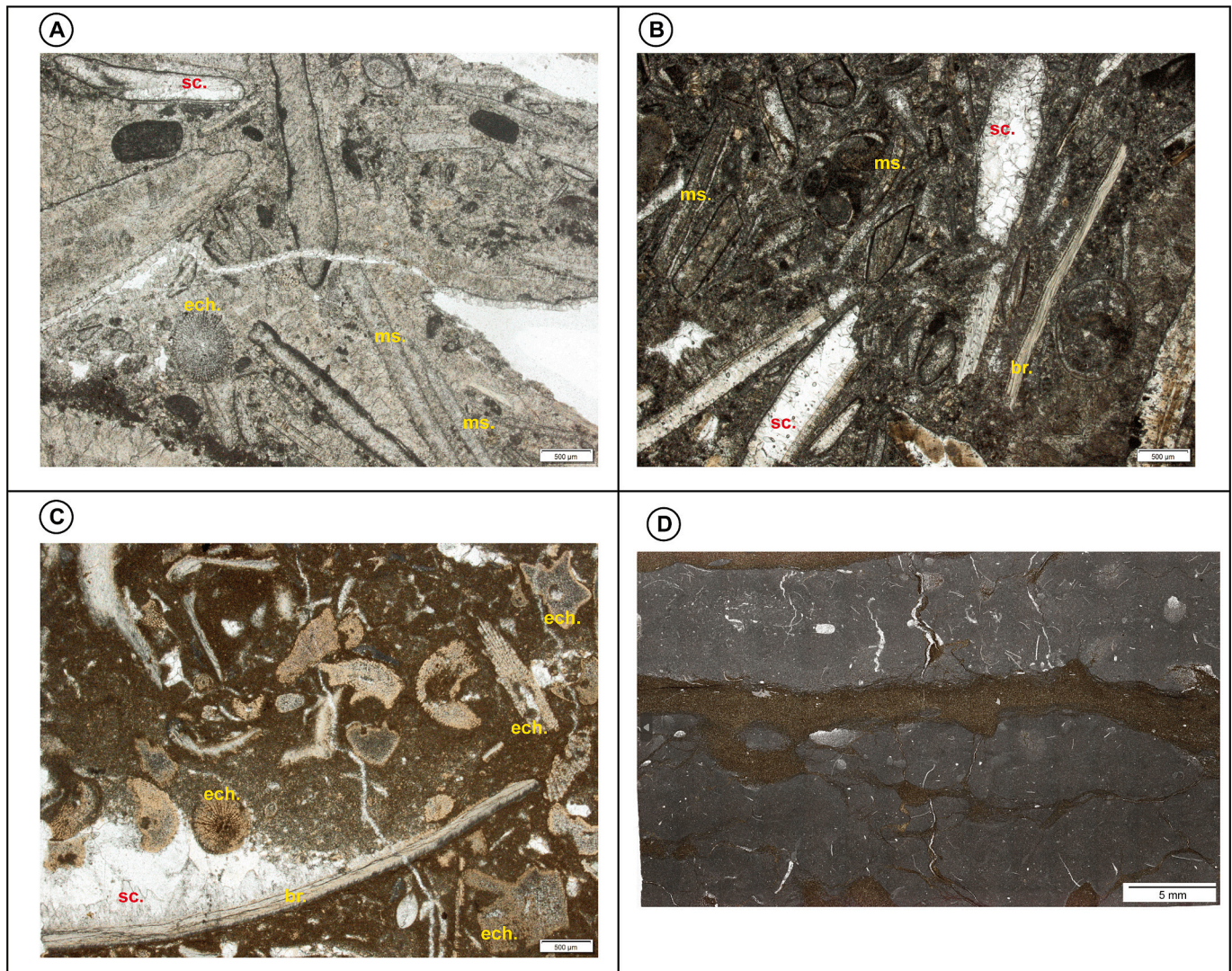


**Fig. 9.** Representative thin section images of hand samples from the studied sections. A) Sample 13C, Jebel Awari, late Smithian – early Spathian. Shell-supported biostrome sample with various skeletal fragments. B) Sample 29C, Jebel Awari, late Smithian. Shell-supported biostrome sample with densely packed skeletal fragments. C) Sample 13C, Wadi Musjah, middle Smithian. Bivalve coquina biostrome sample with abundant echinoderm shell fragments. D) Sample 145C, Qiakong, Spathian. Nodular marly limestone with sponge spicules and brown silty-clay seams. Abbreviations – sc. = sparry calcite, ech. = echinoderm shell, br. = brachiopod shell, ms. = mollusc shell. (For interpretation of the references to colour in this figure legend, the reader is referred to the web version of this article.)

on uranium isotope data (Zhang et al., 2018; Zhang et al., 2019), although it should be noted that there is no evidence for oceanic anoxia during the deposition of the Oman offshore carbonates themselves (Leu et al., 2023). Increase in MSR usually results in higher  $\delta^{18}\text{O}$  values, albeit to a lower extent compared to  $\delta^{34}\text{S}$  (Mizutani and Rafter, 1973; Fichtner et al., 2017). Enhanced MSR rates across the middle Smithian to SSB is thus, also supported by the  $\delta^{18}\text{O}_{\text{CAS}}$  record, which displays an increasing trend during this interval in the studied sections.

The WMJ  $\delta^{34}\text{S}_{\text{CAS}}$  profile (Fig. 6) is thus, at odds with previous suggestions that the middle Smithian negative CIE (N3) was associated with a trend towards lower  $\delta^{34}\text{S}$  values due to causes related to climatic warming (e.g., Song et al., 2014). Similarly, the positive middle Smithian to SSB  $\delta^{34}\text{S}$  trend for WMJ indicates that an increasing  $\delta^{34}\text{S}_{\text{CAS}}$  trend during the Olenekian is not restricted to an interval of climatic cooling e.g., across the SSB. Enhanced nutrient delivery to marine environments across the middle to late Smithian resulted in increased accumulation and burial of OM on continental shelves, as evidenced by black shale deposition during the late Smithian (Widmann et al., 2020; Leu et al., 2022). However, increased OM accumulation and burial during the latest Smithian occurred within a cooling climate regime. As

such, increased marine productivity across the SSB was probably facilitated by enhanced oceanic circulation and upwelling of nutrients from deeper ocean waters (Song et al., 2019). The consequent increased oxygen demand for OM respiration resulted in less oxygenated waters and would have favored increased MSR and pyrite burial in the oceans, as can be inferred from the global positive  $\delta^{13}\text{C}$  and  $\delta^{34}\text{S}$  excursions across the SSB (Fig. 10; Stebbins et al., 2019b).

The SSB increasing  $\delta^{34}\text{S}$  trend for JA and WMJ was followed by a sharp  $\delta^{34}\text{S}$  decrease at the base of the Spathian (UAZ 4) followed by a muted recovery (to higher values but still lower than during the SSB positive excursion) in UAZ 5 (Figs. 5, 6). Based on correlations with the QIA section, the WMJ and JA basal Spathian  $\delta^{34}\text{S}$  decrease is estimated to have spanned ca. 180 kyr and predates the eventual  $\delta^{34}\text{S}$  decrease recorded for other sections during the early Spathian (Fig. 1; Fig. 10). Two hypotheses may explain this negative  $\delta^{34}\text{S}$  trend: 1) localized upwelling of  $\text{H}_2\text{S}$ -rich cold waters in the NeoTethys around the SSB or 2) Post-depositional alteration of the CAS S-isotope compositions of these samples. Several studies have suggested that the SSB was characterized by climatic cooling-mediated oceanic overturning circulation in contrast to the relatively stagnant ocean circulation of the middle Smithian (Lyu

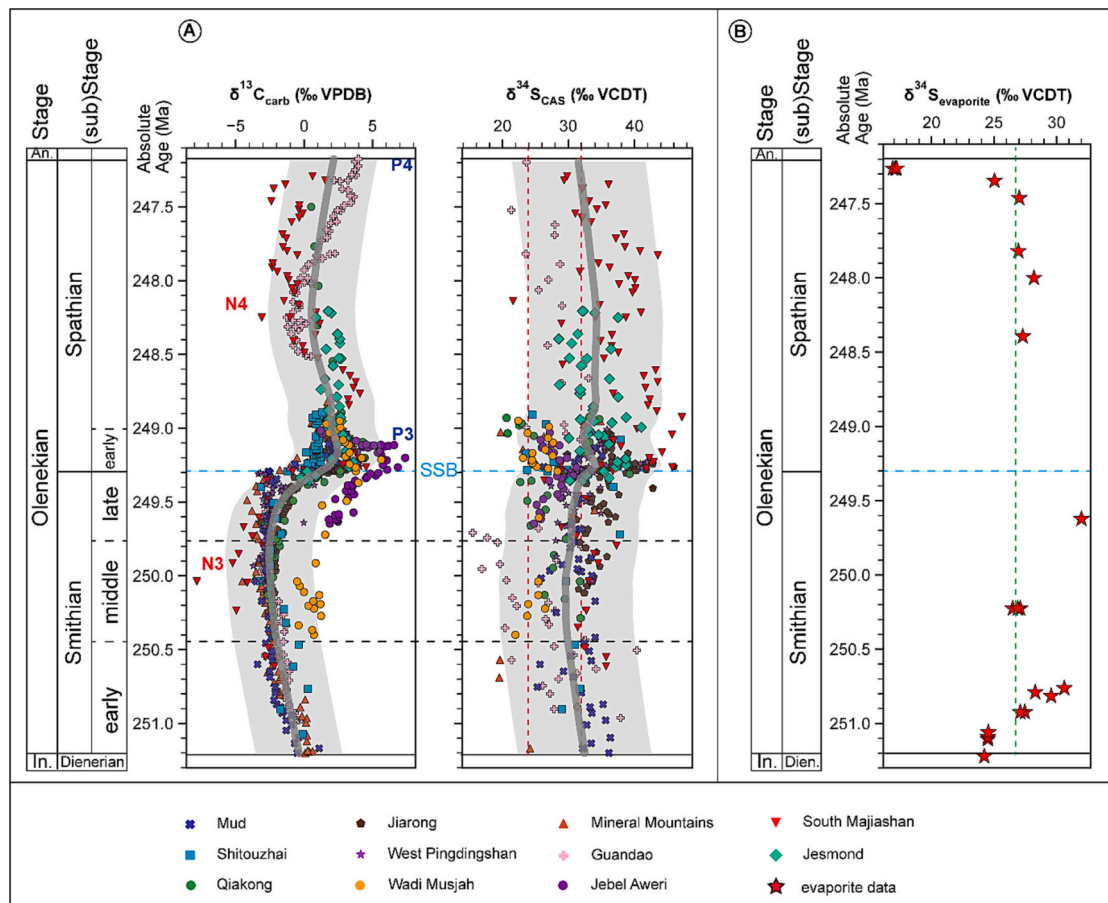


**Fig. 10.** A) Absolute age calibrated compilation of previously published Olenekian  $\delta^{13}\text{C}$  and  $\delta^{34}\text{S}$  records and data from the current study. Literature  $\delta^{13}\text{C}$  and  $\delta^{34}\text{S}$  values are taken from the same sources given in Fig. 1. B) Olenekian evaporite  $\delta^{34}\text{S}$  record as compiled by Present et al. (2020). Absolute ages for the Smithian and Spathian are based on Widmann et al. (2020), Induan – Olenekian boundary and Olenekian – Anisian boundary ages are taken from the International Chronostratigraphic Chart 2023 (Cohen et al., 2013; updated). The nomenclature: N3, N4, P3, P4 depicts globally recognizable carbon isotope excursions after Song et al. (2013). In. = Induan, An. = Anisian. Dashed red lines on the CAS  $\delta^{34}\text{S}$  record depict the range of Olenekian evaporite  $\delta^{34}\text{S}$  values (Present et al., 2020 and references therein). The thick grey lines represent a Lowess regression fit to the data, and the associated grey band represents the 95% confidence interval of the Lowess fit (see supplementary information for details on the implementation of the Lowess fit). The green vertical dashed line in B) depicts the median evaporite  $\delta^{34}\text{S}$  value for the Olenekian (26.7 ‰). (For interpretation of the references to colour in this figure legend, the reader is referred to the web version of this article.)

et al., 2019; Song et al., 2019; Zhang et al., 2015). Both WMJ and JA successions were deposited on offshore topographic highs (i.e., seamounts) (Brühwiler et al., 2012; Leu et al., 2023). As such, the disruption of the flow of offshore currents as they encountered submarine topographic features like seamounts or ridges may have resulted in the upwelling of nutrient- and  $\text{H}_2\text{S}$ -rich deep waters to the surface during the earliest Spathian. Moreover, the  $\text{Ce}_{\text{anom}}$  record for WMJ (Fig. 6) strongly supports an early Spathian ocean oxygenation event, consistent with an inference of oxidation of upwelled  $\text{H}_2\text{S}$ -rich waters producing the  $\delta^{34}\text{S}$  decline recorded. A similar scenario was proposed by Zhang et al. (2015) to explain the negative  $\delta^{34}\text{S}$  excursion recorded at the SSB for the Shitouzhai section. However, this interpretation is argued against by the fact that the basal Spathian  $\delta^{34}\text{S}$  decline is not recorded in other sections (except perhaps, Mud; Fig. 1), which should be the case considering that Early Triassic seawater sulfate concentrations are considered to have been much lower than that of the present day (e.g., Song et al., 2014; Bernasconi et al., 2017; Stebbins et al., 2019b). Hence, it is probably more likely that this negative trend reflects post-depositional alteration of CAS (e.g., via sulfide oxidation or incorporation of different CAS phases during late diagenesis; Johnson et al., 2021). Regardless of the actual explanation of this negative basal Spathian  $\delta^{34}\text{S}$  trend, what is clear is that it is not a global marine  $\delta^{34}\text{S}$  trend.

#### 5.4. Seawater sulfate concentrations during the Olenekian

Quantitative estimates of ancient oceanic sulfate concentrations can be obtained by considering the fractionation between sulfate and sulfide ( $\Delta^{34}\text{S}_{\text{sulfate-sulfide}}$ ) during MSR (the MSR-trend method), as well as the rate of change of sulfate  $\delta^{34}\text{S}$  over a time interval of interest (the rate method; Song et al., 2014; Algeo et al., 2015). The rate method allows for an estimate of the maximum likely  $[\text{SO}_4^{2-}]_{\text{SW}}$  concentration within a time interval of interest, whereas the MSR-trend method enables an estimate of mean  $[\text{SO}_4^{2-}]_{\text{SW}}$  values (Algeo et al., 2015). An estimate of ancient seawater sulfate concentrations based on  $\Delta^{34}\text{S}_{\text{sulfate-sulfide}}$  (MSR-trend method), however, requires an evaluation of the origin of the analyzed pyrite contained in the bulk rock (i.e., whether pyrite is cogenetic or not, and if its isotopic composition is of only local significance). In addition,  $\Delta^{34}\text{S}_{\text{sulfate-sulfide}}$  is dependent on factors other than sulfate concentrations such as organic matter type, sulfate reduction rates and variability between sulfate reducing microbes (Song et al., 2014 and references therein). Alternatively, sulfate concentrations in ancient seawater can be estimated from fluid inclusions in evaporite rocks (e.g., Horita et al., 2002; Lowenstein et al., 2003; see also Turchyn and DePaolo, 2019).

Based on the rate method, Griesbachian – Smithian  $[\text{SO}_4^{2-}]_{\text{SW}}$  concentration within the eastern PaleoTethys was estimated to be between 0.5 and 4.2 mM (Song et al., 2014), with the upper limit of this range being

identical to previous estimates for the Permian – Triassic transition (Luo et al., 2010). Using Griesbachian – Dienerian evaporite  $\delta^{34}\text{S}$  data,  $[\text{SO}_4^{2-}]_{\text{SW}}$  values between 2 and 6 mM were estimated for the Early Triassic using the rate method (Bernasconi et al., 2017). More recently, mean  $[\text{SO}_4^{2-}]_{\text{SW}}$  values between 2.5 and 9.1 mM based on the MSR-trend method have been proposed for the Smithian – Spathian transition using CAS  $\delta^{34}\text{S}$  data for the Jesmond section (Stebbins et al., 2019b).

The absolute age constraint available for our studied sections (Widmann et al., 2020; Leu et al., 2023) permits an estimate of the rates of change of marine  $\delta^{34}\text{S}$  values during the Olenekian. The WMJ and JA dataset considered together (Fig. S14), indicate a  $\delta^{34}\text{S}$  change of ca. +9 ‰ within 1.14 Myr (i.e., between the middle Smithian to SSB), implying a rate of  $\delta^{34}\text{S}$  change of ca. 8 ‰ Myr<sup>-1</sup>. As there are no  $\delta^{34}\text{S}_{\text{CRS}}$  measurements for these sections, a  $\Delta^{34}\text{S}_{\text{CAS-CRS}}$  value of ca. 25 ‰ is assumed based on data for the Jesmond section, considering that this section was deposited in similar paleo-depositional environments as JA and WMJ (i.e., on offshore seamounts, Stebbins et al., 2019b). Based on the estimated rate of  $\delta^{34}\text{S}$  change (8 ‰ Myr<sup>-1</sup>) and a  $\Delta^{34}\text{S}_{\text{CAS-CRS}}$  value of 25 ‰, the rate method is applied to reconstruct Olenekian  $[\text{SO}_4^{2-}]_{\text{SW}}$  values. Using a pyrite burial flux ( $F_{\text{PY}}$ ) of  $4 \times 10^{13}$  g yr<sup>-1</sup> (Song et al., 2014; Algeo et al., 2015) and  $1 \times 10^{14}$  g yr<sup>-1</sup> (Kah et al., 2004), we obtain  $[\text{SO}_4^{2-}]_{\text{SW}}$  values between 2.8 mM and 7.0 mM, respectively for Olenekian seawater. Consequently, it is estimated that Olenekian seawater sulfate concentrations were between 2.8 and 7 mM or between 10 and 25% of the modern  $[\text{SO}_4^{2-}]_{\text{SW}}$  value. This estimated  $[\text{SO}_4^{2-}]_{\text{SW}}$  range is identical to that previously proposed for the Early Triassic based on evaporite S-isotope data and using the rate method (2–6 mM; Bernasconi et al., 2017). The similarity between the CAS- and evaporite-based estimates strengthens the robustness of our estimated Olenekian  $[\text{SO}_4^{2-}]_{\text{SW}}$  concentrations.

Reliable evaporite fluid inclusion estimates of Early Triassic  $[\text{SO}_4^{2-}]_{\text{SW}}$  concentrations are so far lacking (Horita et al., 2002), precluding a direct comparison of our CAS-based Olenekian  $[\text{SO}_4^{2-}]_{\text{SW}}$  concentration estimates with those from coeval evaporite fluid inclusion data. However, estimates of  $[\text{SO}_4^{2-}]_{\text{SW}}$  concentration based on  $\text{SO}_4^{2-}$  content of fluid inclusions in halite deposits suggest that Middle Triassic (Ladinian) and Late Triassic (upper Carnian) seawater had minimum  $[\text{SO}_4^{2-}]_{\text{SW}}$  concentrations of 14 and 13 mM, respectively (Horita et al., 2002; Lowenstein et al., 2003). Considering the upper threshold of our Olenekian  $[\text{SO}_4^{2-}]_{\text{SW}}$  concentration estimate (7 mM),  $[\text{SO}_4^{2-}]_{\text{SW}}$  concentrations may have doubled between the Early Triassic (early Spathian, ca. 249 Ma) and Middle Triassic (Ladinian, ca. 240 Ma).

A question that arises given low Olenekian  $[\text{SO}_4^{2-}]_{\text{SW}}$  estimates is whether there would have been enough sulfate in Olenekian oceans to sustain MSR and pyrite burial over the middle Smithian to SSB, an interval of ca. 1.1 Myr. However, Olenekian Sr isotope records as well as increased clastic deposition during the middle to late Smithian (Sedlacek et al., 2014; Song et al., 2015; Widmann et al., 2020) suggest that sulfate input fluxes via continental weathering likely increased during this interval. Also, mercury records (Shen et al., 2019; Edward et al., 2024b) and volcanic ash occurrence (Ovtcharova et al., 2006; Galfetti et al., 2007a; Widmann et al., 2020) are consistent with a scenario of increased volcanic sulfur input to the ocean-atmosphere system across the Smithian – Spathian transition. Furthermore, it has been suggested that the rate of change of oceanic S-isotope composition need not necessarily be coupled to sulfate concentrations if open ocean environments are the locus of pyrite burial instead of shelf settings (Rennie et al., 2018). However, it is currently unclear if this was the case during the Early Triassic. In addition,  $\Delta^{34}\text{S}_{\text{CAS-CRS}}$  data from the open ocean Jesmond section suggest that  $[\text{SO}_4^{2-}]_{\text{SW}}$  concentrations remained constant across the SSB (Stebbins et al., 2019b). Based on these considerations, we suggest that seawater sulfate depletion due to MSR and pyrite burial was probably offset by sustained sulfate input fluxes during this interval.

## 5.5. Sulfur cycle box modeling constraints

To quantitatively constrain potential controls on the Olenekian marine sulfur cycle variations as recorded in the current study, simple sulfur cycle box model experiments were conducted to 1) explore the magnitude of change in the input and output fluxes of the sulfur cycle that are compatible with the magnitude and duration of the Olenekian  $\delta^{34}\text{S}$  changes recorded, 2) evaluate the extent of sulfate-sulfide fractionation ( $\Delta^{34}\text{S}_{\text{sulfate-sulfide}}$ ) that is compatible with the recorded CAS  $\delta^{34}\text{S}$  trend and 3) assess the seawater sulfate concentrations that are consistent with the  $\delta^{34}\text{S}$  variations. The box model used is a simple time-dependent sulfur cycle model described in Witts et al. (2018), which solves a system of two differential equations for the concentration and isotopic composition of marine sulfate as follows:

$$\frac{\partial S}{\partial t} = W_{\text{PYR}} + W_{\text{GYP}} - B_{\text{PYR}} - B_{\text{GYP}} \quad (6)$$

$$\frac{\partial(S \times \delta S)}{\partial t} = W_{\text{PYR}}\delta_{\text{PYR}} + W_{\text{GYP}}\delta_{\text{GYP}} - B_{\text{PYR}}(\delta_S - \Delta S) - B_{\text{GYP}}\delta_S \quad (7)$$

$W_{\text{PYR}}$  is the weathering flux of pyrite ( $0.7 \times 10^{12}$  mol/yr; He et al., 2020),  $W_{\text{GYP}}$  is the weathering flux of gypsum ( $1 \times 10^{12}$  mol/yr; He et al., 2020),  $B_{\text{PYR}}$  is the burial flux of pyrite (varied in experiments, initial set to  $W_{\text{PYR}}$  value),  $B_{\text{GYP}}$  is the burial rate of gypsum ( $W_{\text{GYP}} \left( \frac{S}{S_{\text{steady}}} \right)$ ),  $S_{\text{steady}}$  is the oceanic sulphate concentration at equilibrium (varied in experiments),  $\delta_{\text{PYR}}$  and  $\delta_{\text{GYP}}$  are the respective isotopic compositions of pyrite and gypsum ( $\delta_{\text{PYR}} = -20$  ‰, Paytan et al. (1998);  $\delta_{\text{GYP}} = 20$  ‰, Holser and Kaplan, 1966), and  $\Delta S$  is the sulfur enrichment factor (varied in experiments).

Eq. (6) represents the input and output fluxes of marine sulfate via burial and weathering. The S-isotope composition of seawater sulfate is resolved by computing  $\delta S = \frac{(S \times \delta S)}{S}$  (Witts et al., 2018). Eqs. (6) and (7) are solved in Python using a 4th order Runge-Kutta method. In the model experiments, we use  $\Delta^{34}\text{S}_{\text{CAS-CRS}}$  to represent the fractionation between sulfate and sulfide (i.e.,  $\Delta S$  in the model). Two scenarios are tested, using  $\Delta S = 25$  ‰ (Stebbins et al., 2019b) and  $\Delta S = 44$  ‰ (median  $\Delta^{34}\text{S}_{\text{CAS-CRS}}$  value for the QIA dataset). Seawater sulfate concentrations (the model parameter:  $S_{\text{steady}}$ ) were varied between 2.8 mM and 14 mM (i.e., the lower limit from our rate method calculations and the Middle Triassic evaporite fluid inclusion estimate). Results from the model experiments are presented in Fig. 11.

We also estimated the expected increase in organic carbon burial during the late Smithian using the  $\delta^{13}\text{C}$  record after Kump and Arthur (1999) based on the following equation:

$$f_{\text{org}} = \frac{\delta_w - \delta_{\text{carb}}}{\Delta_B} \quad (8)$$

$f_{\text{org}}$  = fraction of buried organic carbon,  $\delta_w$  = mantle  $\delta^{13}\text{C}$  (–5 ‰; Kump and Arthur, 1999),  $\delta_{\text{carb}}$  = carbonate  $\delta^{13}\text{C}$ , and  $\Delta_B$  = difference between organic and carbonate  $\delta^{13}\text{C}$  (for QIA = –29 ‰; Widmann, 2019). Based on the 6 ‰ positive CIE across the late Smithian to early Spathian (Widmann et al., 2020), organic carbon burial can be estimated to have increased by 200% by the SSB. Considering that the rates of organic carbon and pyrite burial in non-euxinic marine sediments (such as those herein studied) have a constant ratio (Bernier and Raiswell, 1983), pyrite burial would have increased at most by a factor of 3 during the late Smithian.

In this case, model simulations indicate that an overall 9 ‰  $\delta^{34}\text{S}$  increase over 1.14 Myr recorded for the Oman offshore sections within the middle Smithian to SSB are only compatible with seawater sulfate concentrations around 2.8 mM and  $\Delta S$  of 25 ‰ considering pyrite burial rate increase of 200% as estimated during this interval (Fig. 11). Alternatively sulfate concentrations closer to 7 mM are required for  $\Delta S$  of 44 ‰ with the same rate of pyrite burial increase. As such, modeling constraints indicate that with either estimated  $\Delta^{34}\text{S}_{\text{sulfate-sulfide}}$  of 25 ‰

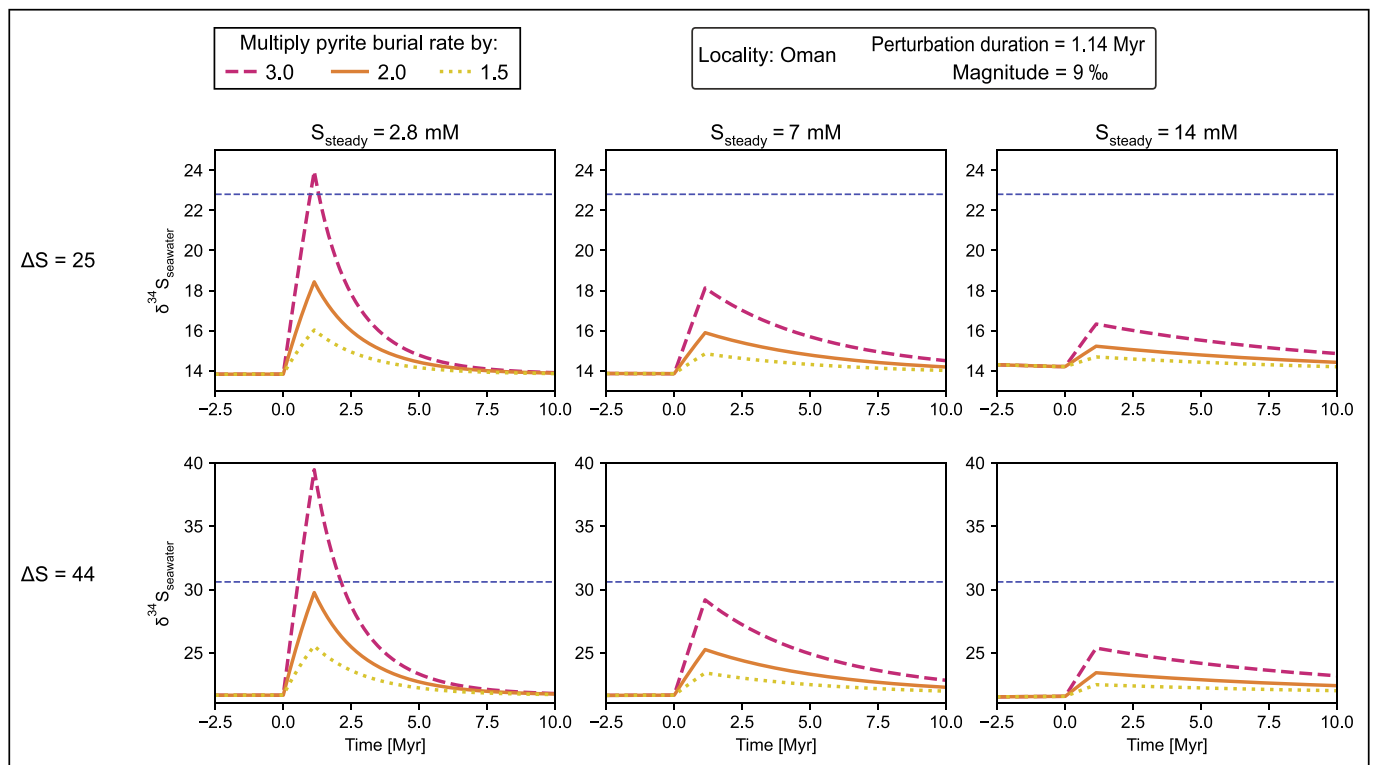


**Fig. 11.** Sulfur cycle box modeling results showing the changes in pyrite burial fluxes required to reproduce the middle Smithian to Smithian – Spathian boundary (SSB)  $\delta^{34}\text{S}$  increase recorded. The horizontal, blue, dashed lines mark the  $\delta^{34}\text{S}$  peak value relative to equilibrium  $\delta^{34}\text{S}$  values predicted by the model for  $\Delta\text{S} = 25\text{‰}$  (13.8 ‰) and  $\Delta\text{S} = 44\text{‰}$  (21.6 ‰). (For interpretation of the references to colour in this figure legend, the reader is referred to the web version of this article.)

or values closer to that of average modern seawater (i.e., around 40 ‰; Bernasconi et al., 2017 and references therein), a much lower marine sulfate reservoir (in this case, 2.8–7 mM) is required for the magnitude and duration of the observed  $\delta^{34}\text{S}$  increase. Consequently, given the compatibility of the rate method seawater sulfate concentration estimates with results from box model simulations, we propose that seawater sulfate concentrations during the Olenekian in the Tethys were at maximum  $\sim 7$  mM or  $< 25\%$  of the modern seawater value. This  $[\text{SO}_4^{2-}]_{\text{SW}}$  value is similar to the upper limit of the  $[\text{SO}_4^{2-}]_{\text{SW}}$  range (2–6 mM) proposed for the Early Triassic based on evaporite  $\delta^{34}\text{S}$  data (Bernasconi et al., 2017).

### 5.6. Implications for Olenekian marine faunal perturbations

Previous studies have suggested a causal link between faunal extinction around the SSB and the development of oceanic anoxia (e.g., Sun et al., 2015; Song et al., 2019). However, nekto-pelagic organisms, like conodonts and ammonoids, seem to have been less affected by late Smithian extinction than benthic communities (Stanley, 2007, 2008). Even marine level-bottom communities were likely not primarily impacted by marine environmental perturbations during the Early Triassic. Instead, the diversification pattern of most taxa and guilds shows an initial Early Triassic lag phase followed by a hyperbolic diversity increase during the early middle Anisian and was mainly driven by the intensity of biotic interactions (Friesenbichler et al., 2021).

Comparison of the current  $\delta^{34}\text{S}$  record with the most recent analysis of conodont diversity in the studied successions (Leu et al., 2022; Leu et al., 2023) indicates that phases of increased nektonic faunal extinction and diversification alike coincide with the global middle Smithian to SSB  $\delta^{34}\text{S}$  increase (interpreted as reflecting continuous depletion of water column dissolved oxygen, Figs. 4–6). Also, black shale deposition (suggestive of more reducing conditions) in QIA and coeval sections in the Nanpanjiang Basin, South China (Widmann et al., 2020; this study)

coincides with both a conodont extinction phase and the onset of a diversification pulse at the end of the black shale interval (Fig. 4; Leu et al., 2022). Furthermore, the middle Smithian was marked by climatic warming followed by cooling at the SSB, as evidenced by sea surface temperature records (Romano et al., 2013; Goude mand et al., 2019). However, the warm middle Smithian interval was also characterized by a peak in Early Triassic ammonoid diversity (Brayard et al., 2006; Brühwiler et al., 2010; Brosse et al., 2013). These observations are at variance with the notion that oceanic anoxia or seawater temperature changes alone can explain faunal turnover during the Olenekian. Although, faunal diversification in the earliest Spathian did coincide with ocean oxygenation (Fig. 6) and seawater temperature decrease (Goude mand et al., 2019). It is important to note that various abiotic (and biotic) factors, apart from dissolved oxygen levels, can act as stressors and impact the diversification rates of conodonts and their paleobiogeographic distribution (Goude mand et al., 2019; Leu et al., 2019). A recent study by Herrmann et al. (2015) indicates that the distribution of conodont biofacies was influenced by more physico-chemical properties than dissolved oxygen levels, such as salinity and nutrients. Furthermore, it has been suggested that Early Triassic conodont biodiversity changes were predominantly impacted by both sea level and sea temperature fluctuations (Leu et al., 2019; Ginot and Goude mand, 2020). Additionally, Jattiot et al. (2018) proposed that sedimentary facies and depositional environment (i.e., vertically diverse graben-horst structures vs. vertically homogenous continental shelf areas) were the main influencers of the taxonomic composition of Smithian ammonoid assemblages. Taken together, the above enumerated considerations, as well as our data, suggest that marine dissolved oxygen levels alone are unlikely to explain the faunal perturbations that characterized the Smithian to Spathian transition. Instead, a combination of biotic and abiotic factors (such as nutrients, predation stress, intraspecific competition, and sea-level changes) probably influenced the Smithian – Spathian transition marine faunal perturbations, in

agreement with previous similar suggestions (e.g., Herrmann et al., 2015; Jattiot et al., 2018; Goudemand et al., 2019).

## 6. Conclusions

The evolution of marine  $\delta^{34}\text{S}$  across the middle Smithian to Spathian (Olenekian) are documented in the current study from continental shelf (QIA) and offshore (WMJ and JA) carbonate successions. Detailed assessments of the preservation of primary CAS isotopic information within the studied successions as well as comparisons with the sparse evaporite  $\delta^{34}\text{S}$  record, allow us to conclude that the CAS isotopic compositions for the QIA section suffer from post-depositional alteration. However, near primary marine S-isotope compositions are mostly preserved by the offshore carbonates. In addition, an assessment of published Olenekian CAS  $\delta^{34}\text{S}$  records relative to contemporaneous evaporite data suggests that the Olenekian CAS record only partially reflects primary seawater  $\delta^{34}\text{S}$  values. The CAS record nonetheless preserves a primary global trend of increasing seawater  $\delta^{34}\text{S}$  values across the middle Smithian to SSB followed by a gradual  $\delta^{34}\text{S}$  decline during the Spathian. The middle Smithian – SSB global increasing  $\delta^{34}\text{S}$  trend, observed also in our studied sections, is consistent with a global decrease in ocean dissolved oxygen and an increase in microbial sulfate reduction and pyrite burial. Other short-term variability in the CAS isotopic data, including a sharp  $\delta^{34}\text{S}$  decrease at the basal Spathian observed for WMJ and JA, are interpreted as most likely reflective of post-depositional alteration of CAS.

Based on sulfur cycling rate calculations and box modeling experiments, the inferred global sulfur cycle perturbations occurred within the context of a Olenekian seawater sulfate inventory that was between 10 and 25% (2.8–7 mM) of that of modern seawater. Furthermore, results from the current study suggest that variations in oceanic dissolved oxygen levels, inferred from the  $\delta^{34}\text{S}$  and REE data, are not consistently correlated to nektonic faunal changes during the Smithian to Spathian interval in the studied sections.

## CRedit authorship contribution statement

**Oluwaseun Edward:** Conceptualization, Data curation, Formal analysis, Investigation, Visualization, Writing – original draft, Writing – review & editing. **Jorge E. Spangenberg:** Investigation, Methodology, Resources, Validation, Writing – review & editing. **Marc Leu:** Data curation, Resources, Validation, Writing – review & editing. **Charline Ragon:** Investigation, Software, Writing – review & editing. **Sandrine Le Houedec:** Investigation, Methodology, Writing – review & editing. **Aymon Baud:** Investigation, Methodology, Writing – review & editing. **Hugo Bucher:** Funding acquisition, Project administration, Resources, Writing – review & editing. **Torsten Vennemann:** Conceptualization, Funding acquisition, Project administration, Resources, Supervision, Writing – review & editing.

## Declaration of competing interest

The authors declare that they have no known competing financial interests or personal relationships that could have appeared to influence the work reported in this paper.

## Data availability

The dataset generated for this article can be found at <https://dx.doi.org/10.17632/p5238ks2m5.3>, an open-source online data repository hosted at Mendeley Data (Edward et al., 2024).

## Acknowledgements

The authors thank Claudia Baumgartner, Laetitia Monbaron, Maxime Siegenthaler and Jessica Chaves (UNIL) for laboratory support. This

study was funded by a Swiss National Science Foundation Sinergia Grant (Project Number: CRSII5\_180253). SLH acknowledges financial support by the University of Geneva (S18173). Three anonymous reviewers are thanked for their constructive comments which improved the manuscript.

## Appendix A. Supplementary data

Supplementary data to this article can be found online at <https://doi.org/10.1016/j.chemgeo.2024.121984>.

## References

- Algeo, T.J., Luo, G.M., Song, H.Y., Lyons, T.W., Canfield, D.E., 2015. Reconstruction of secular variation in seawater sulfate concentrations. *Biogeosciences* 12, 2131–2151. <https://doi.org/10.5194/bg-12-2131-2015>.
- Algeo, T.J., Brayard, A., Richoz, S., 2019. The Smithian-Spathian boundary: a critical juncture in the early Triassic recovery of marine ecosystems. *Earth Sci. Rev.* 195, 1–6. <https://doi.org/10.1016/j.earscirev.2019.102877>.
- Alibo, D.S., Nozaki, Y., 1999. Rare earth elements in seawater: particle association, shale-normalization, and Ce oxidation. *Geochim. Cosmochim. Acta* 63, 363–372. [https://doi.org/10.1016/S0016-7037\(98\)00279-8](https://doi.org/10.1016/S0016-7037(98)00279-8).
- Bagherpour, B., Bucher, H., Baud, A., Brosse, M., Vennemann, T., Martini, R., Guodun, K., 2017. Onset, development, and cessation of basal early Triassic microbialites (BETM) in the Nanpanjiang pull-apart Basin, South China Block. *Gondwana Res.* 44, 178–204. <https://doi.org/10.1016/j.gr.2016.11.013>.
- Bagherpour, B., Bucher, H., Vennemann, T., Schneebeil-Hermann, E., Yuan, D.X., Leu, M., Zhang, C., Shen, S.Z., 2020. Are late Permian carbon isotope excursions of local or of global significance? *Geol. Soc. Am. Bull.* 132, 521–544. <https://doi.org/10.1130/B31996.1>.
- Bagnoud-Velásquez, M., Spangenberg, J.E., Poiré, D.G., Gómez Peral, L.E., 2013. Stable isotope (S, C) chemostratigraphy and hydrocarbon biomarkers in the Ediacaran upper section of Sierras Bayas Group, Argentina. *Precambrian Res.* 231, 388–400. <https://doi.org/10.1016/j.precamres.2013.04.001>.
- Barkan, Y., Paris, G., Webb, S.M., Adkins, J.F., Halesy, I., 2020. Sulfur isotope fractionation between aqueous and carbonate-associated sulfate in abiotic calcite and aragonite. *Geochim. Cosmochim. Acta* 280, 317–339. <https://doi.org/10.1016/j.gca.2020.03.022>.
- Baud, A., 2013. The Olenekian (early Triassic) Red Ammonoid Limestone, a time-specific facies on the Gondwana margin: Timor-Roof of the World-Oman connection. *Acta Geol. Sin.* 87, 894–931. <https://doi.org/10.1111/1755-6724.12150.2>.
- Baud, A., Béchenneq, F., Krystyn, L., Le Métour, J., Marcoux, J., Maury, R., Richoz, S., 2001. Permo-Triassic Deposits: from the Platform to the Basin and Seamounts. Conference on the Geology of Oman, Field guidebook, Excursion A01, Conference on the Geology of Oman, Field guidebook, Excursion A01, pp. 1–54. <https://www.researchgate.net/publication/236624812>.
- Bernasconi, S.M., Meier, I., Wohlwend, S., Brack, P., Hochuli, P.A., Bläsi, H., Wortmann, U.G., Ramseyer, K., 2017. An evaporite-based high-resolution sulfur isotope record of late Permian and Triassic seawater sulfate. *Geochim. Cosmochim. Acta* 204, 331–349.
- Berner, R.A., 1987. Models for carbon and sulfur cycles and atmospheric oxygen; application to Paleozoic geologic history. *Am. J. Sci.* 287, 177–196. <https://doi.org/10.2475/ajs.287.3.177>.
- Berner, R.A., Raiswell, R., 1983. Burial of organic carbon and pyrite sulfur in sediments over Phanerozoic time: a new theory. *Geochim. Cosmochim. Acta* 47, 855–862. [https://doi.org/10.1016/0016-7037\(83\)90151-5](https://doi.org/10.1016/0016-7037(83)90151-5).
- Bottrell, S.H., Newton, R.J., 2006. Reconstruction of changes in global sulfur cycling from marine sulfate isotopes. *Earth Sci. Rev.* 75, 59–83. <https://doi.org/10.1016/j.earscirev.2005.10.004>.
- Brayard, A., Bucher, H., Escarguel, G., Fluteau, F., Bourquin, S., Galfetti, T., 2006. The early Triassic ammonoid recovery: Paleoclimatic significance of diversity gradients. *Palaeogeogr. Palaeoclimatol. Palaeoecol.* 239, 374–395. <https://doi.org/10.1016/j.palaeo.2006.02.003>.
- Brosse, M., Brayard, A., Fara, E., Neige, P., 2013. Ammonoid recovery after the Permian-Triassic mass extinction: a re-exploration of morphological and phylogenetic diversity patterns. *J. Geol. Soc. Lond.* 170, 225–236. <https://doi.org/10.1144/jgs2012-084>.
- Brühwiler, T., Bucher, H., Brayard, A., Goudemand, N., 2010. High-resolution biochronology and diversity dynamics of the early Triassic ammonoid recovery: the Smithian faunas of the Northern Indian margin. *Palaeogeogr. Palaeoclimatol. Palaeoecol.* 297, 491–501. <https://doi.org/10.1016/j.palaeo.2010.09.001>.
- Brühwiler, T., Bucher, H., Goudemand, N., Galfetti, T., 2012. Smithian (early Triassic) ammonoid faunas from Exotic Blocks from Oman: taxonomy and biochronology. *Palaeontogr. Abt. A: Palaeozoolog.-Stratigr.* 296, 3–107. <https://doi.org/10.1127/pala/296/2012/3>.
- Burdett, J.W., Arthur, M.A., Richardson, M., 1989. A Neogene seawater sulfur isotope age curve from calcareous pelagic microfossils. *Earth Planet. Sci. Lett.* 94, 189–198. [https://doi.org/10.1016/0012-821x\(89\)90138-6](https://doi.org/10.1016/0012-821x(89)90138-6).
- Canfield, D.E., Raiswell, R., Westrich, J.T., Reaves, C.M., Berner, R.A., 1986. The use of chromium reduction in the analysis of reduced inorganic sulfur in sediments and shales. *Chem. Geol.* 54, 149–155. [https://doi.org/10.1016/0009-2541\(86\)90078-1](https://doi.org/10.1016/0009-2541(86)90078-1).

- Claypool, G.E., Holser, W.T., Kaplan, I.R., Sakai, H., Zak, I., 1980. The age curves of sulfur and oxygen isotopes in marine sulfate and their mutual interpretation. *Chem. Geol.* 28, 199–260. [https://doi.org/10.1016/0009-2541\(80\)90047-9](https://doi.org/10.1016/0009-2541(80)90047-9).
- Cohen, K.M., Finney, S.C., Gibbard, P.L., Fan, J.X., 2013. Updated. The ICS International Chronostratigraphic Chart. *International Union of Geological Sciences*, vol. 36, pp. 199–204. <https://doi.org/10.18814/epiuiugs/2013/v36i3/002>.
- Cortecci, G., Reyes, E., Berti, G., Casati, P., 1981. Sulfur and oxygen isotopes in Italian marine sulfates of Permian and Triassic ages. *Chem. Geol.* 34, 65–79. [https://doi.org/10.1016/0009-2541\(81\)90072-3](https://doi.org/10.1016/0009-2541(81)90072-3).
- De Baar, H.J.W., Bacon, M.P., Brewer, P.G., Bruland, K.W., 1985. Rare earth elements in the Pacific and Atlantic Oceans. *Geochim. Cosmochim. Acta* 49, 1943–1959. [https://doi.org/10.1016/0016-7037\(85\)90089-4](https://doi.org/10.1016/0016-7037(85)90089-4).
- Du, Y., Song, H., Algeo, T.J., Song, H., Tian, L., Chu, D., Shi, W., Li, C., Tong, J., 2022. A massive magmatic degassing event drove the Late Smithian Thermal Maximum and Smithian–Spathian boundary mass extinction. *Glob. Planet. Chang.* 215, 103878 <https://doi.org/10.1016/j.gloplacha.2022.103878>.
- Edward, Oluwaseun, Spangenberg, Jorge, Leu, Marc, Ragon, Charline, Le Houedec, Sandrine, Baud, Aymon, Bucher, Hugo, Vennemann, Torsten, 2024a. CAS isotopic and rare earth element concentration data for Olenekian carbonate rocks from Qiakong, Wadi Musjah and Jebel Aweri sections. *Mendeley Data V3*. 10.17632/p5238ks2m5.3.
- Edward, O., Leu, M., Bucher, H., Le Houedec, S., Blattmann, F., V  rard, C., Adatte, T., Baud, A., Sonke, J.E., Vennemann, T., 2024b. Evidence for variable provenance of Mercury anomalies during the Smithian–Spathian (Olenekian). *Glob. Planet. Chang.* 232, 104343 <https://doi.org/10.1016/j.gloplacha.2023.104343>.
- Fichtner, V., Strauss, H., Immenhauser, A., Buhl, D., Neuser, R.D., Niedermayr, A., 2017. Diagenesis of carbonate associated sulfate. *Chem. Geol.* 463, 61–75. <https://doi.org/10.1016/j.chemgeo.2017.05.008>.
- Friesenbichler, E., Hautmann, M., Bucher, H., 2021. The main stage of recovery after the end-Permian mass extinction: Taxonomic rediversification and ecologic reorganization of marine level-bottom communities during the Middle Triassic. *PeerJ* 9, e11654. <https://doi.org/10.7717/peerj.11654>.
- Galfetti, T., Bucher, H., Ovtcharova, M., Schaltegger, U., Brayard, A., Br  hwiler, T., Goudemand, N., Weissert, H., Hochuli, P.A., Cordey, F., 2007a. Timing of the Early Triassic carbon cycle perturbations inferred from new U–Pb ages and ammonoid biochronozones. *Earth Planet. Sci. Lett.* 258, 593–604.
- Galfetti, T., Hochuli, P.A., Brayard, A., Bucher, H., Weissert, H., Vigran, J.O., 2007b. Smithian–Spathian boundary event: evidence for global climatic change in the wake of the end-Permian biotic crisis. *Geology* 35, 291–294. <https://doi.org/10.1130/G23117A.1>.
- German, C.R., Elderfield, H., 1990. Application of the Ce anomaly as a paleoredox indicator: the ground rules. *Paleoceanography* 5, 823–833. <https://doi.org/10.1029/PA005i005p00823>.
- Gill, B.C., Lyons, T.W., Saltzman, M.R., 2007. Parallel, high-resolution carbon and sulfur isotope records of the evolving Paleozoic marine sulfur reservoir. *Palaeogeogr. Palaeoclimatol. Palaeoecol.* 256, 156–173. <https://doi.org/10.1016/j.palaeo.2007.02.030>.
- Gill, B.C., Lyons, T.W., Frank, T.D., 2008. Behavior of carbonate-associated sulfate during meteoric diagenesis and implications for the sulfur isotope paleoproxy. *Geochim. Cosmochim. Acta* 72, 4699–4711. <https://doi.org/10.1016/j.gca.2008.07.001>.
- Ginot, S., Goudemand, N., 2020. Global climate changes account for the main trends of conodont diversity but not for their final demise. *Glob. Planet. Chang.* 195, 103325 <https://doi.org/10.1016/j.gloplacha.2020.103325>.
- Goudemand, N., Romano, C., Leu, M., Bucher, H., Trotter, J.A., Williams, I.S., 2019. Dynamic interplay between climate and marine biodiversity upheavals during the early Triassic Smithian–Spathian biotic crisis. *Earth Sci. Rev.* 195, 169–178. <https://doi.org/10.1016/j.earscirev.2019.01.013>.
- Habicht, K.S., Canfield, D.E., 1996. Sulphur isotope fractionation in modern microbial mats and the evolution of the Sulphur cycle. *Nature* 382, 342–343. <https://doi.org/10.1038/382342a0>.
- Halevy, I., Peters, S.E., Fischer, W.W., 2012. Sulfate Burial Constraints on the Phanerozoic Sulfur Cycle. *Science* 337, 331–334. <https://doi.org/10.1126/science.1220224>.
- Harris, C.R., Millman, K.J., van der Walt, S.J., Gommers, R., Virtanen, P., Cournapeau, D., Wieser, E., Taylor, J., Berg, S., Smith, N.J., Kern, R., Picus, M., Hoyer, S., van Kerkwijk, M.H., Brett, M., Haldane, A., del R  o, J.F., Wiebe, M., Peterson, P., G  rard-Marchant, P., Sheppard, K., Reddy, T., Weckesser, W., Abbasi, H., Gohlke, C., Oliphant, T.E., 2020. Array programming with NumPy. *Nature* 585, 357–362. <https://doi.org/10.1038/s41586-020-2649-2>.
- Hausner, M., Martini, R., Burns, S., Dumitrica, P., Krystyn, L., Matter, A., Peters, T., Zaninetti, L., 2001. Triassic stratigraphic evolution of the Arabian–Greater India embayment of the southern Tethys margin. *Eclogae Geol. Helv.* 94, 29–62. <https://doi.org/10.5169/seals-168876>.
- He, T., Dal Corso, J., Newton, R.J., Wignall, P.B., Mills, B.J.W., Todaro, S., Di Stefano, P., Turner, E.C., Jamieson, R.A., Randazzo, V., Rigo, M., Jones, R.E., Dunhill, A.M., 2020. An enormous sulfur isotope excursion indicates marine anoxia during the end-Triassic mass extinction. *Sci. Adv.* 6, eabb6704. <https://doi.org/10.1126/sciadv.abb6704>.
- Hermann, E., Hochuli, P.A., Bucher, H., Br  hwiler, T., Hautmann, M., Ware, D., Roohi, G., 2011. Terrestrial ecosystems on North Gondwana following the end-Permian mass extinction. *Gondwana Res.* 20, 630–637. <https://doi.org/10.1016/j.gr.2011.01.008>.
- Herrmann, A.D., Barrick, J.E., Algeo, T.J., 2015. The relationship of conodont biofacies to spatially variable water mass properties in the late Pennsylvanian Midcontinent Sea. *Paleoceanography* 30, 269–283. <https://doi.org/10.1002/2014PA002725>.
- Holser, W.T., 1977. Catastrophic chemical events in the history of the ocean. *Nature* 267, 403–408. <https://doi.org/10.1038/267403a0>.
- Holser, W.T., Kaplan, I.R., 1966. Isotope geochemistry of sedimentary sulfates. *Chem. Geol.* 1, 93–135. [https://doi.org/10.1016/0009-2541\(66\)90011-8](https://doi.org/10.1016/0009-2541(66)90011-8).
- Holser, W.T., Schidlowski, M., Mackenzie, F., Maynard, J., 1988. Geochemical cycles of carbon and sulfur. In: Gregor, C.B., Garrels, R.M., Mackenzie, F., Maynard, J.B. (Eds.), *Chemical Cycles in the Evolution of the Earth*. John Wiley & Sons, New York, pp. 105–173.
- Horacek, M., Brandner, R., Richoz, S., Povoden-Karadeniz, E., 2010. Lower Triassic Sulphur isotope curve of marine sulphates from the Dolomites, N-Italy. *Palaeogeogr. Palaeoclimatol. Palaeoecol.* 290, 65–70. <https://doi.org/10.1016/j.palaeo.2010.02.016>.
- Horita, J., Zimmermann, H., Holland, H.D., 2002. Chemical evolution of seawater during the Phanerozoic: Implications from the record of marine evaporites. *Geochim. Cosmochim. Acta* 66, 3733–3756. [https://doi.org/10.1016/S0016-7037\(01\)00884-5](https://doi.org/10.1016/S0016-7037(01)00884-5).
- Hurtgen, M.T., Arthur, M.A., Suits, N.S., Kaufman, A.J., 2002. The sulfur isotopic composition of Neoproterozoic seawater sulfate: implications for a snowball Earth? *Earth Planet. Sci. Lett.* 203, 413–429. [https://doi.org/10.1016/S0012-821X\(02\)00804-X](https://doi.org/10.1016/S0012-821X(02)00804-X).
- Insalaco, E., Virgone, A., Courme, B., Gaillot, J., Kamali, M., Moallemi, A., Lotpour, M., Monibi, S., 2006. Upper Dalan Member and Kangan Formation between the Zagros Mountains and offshore Fars, Iran: depositional system, biostratigraphy and stratigraphic architecture. *GeoArabia* 11, 75–176. <https://doi.org/10.2113/geoarabia110275>.
- Jattiot, R., Brayard, A., Bucher, H., Vennin, E., Caravaca, G., Jenks, J.F., Bylund, K.G., Escarguel, G., 2018. Palaeobiogeographical distribution of Smithian (early Triassic) ammonoid faunas within the western USA basin and its controlling parameters. *Palaeontology* 61, 881–904. <https://doi.org/10.1111/pala.12375>.
- Johnson, D.L., Present, T.M., Li, M., Shen, Y., Adkins, J.F., 2021. Carbonate associated sulfate (CAS)  $\delta^{34}\text{S}$  heterogeneity across the End-Permian Mass Extinction in South China. *Earth Planet. Sci. Lett.* 574, 117172 <https://doi.org/10.1016/j.epsl.2021.117172>.
- J  rgensen, B.B., 1982. Mineralization of organic matter in the sea bed—the role of sulphate reduction. *Nature* 296, 643–645. <https://doi.org/10.1038/296643a0>.
- J  rgensen, B.B., Findlay, A.J., Pellerin, A., 2019. The Biogeochemical Sulfur Cycle of Marine Sediments. *Front. Microbiol.* 10 <https://doi.org/10.3389/fmicb.2019.00849>.
- Kah, L.C., Lyons, T.W., Frank, T.D., 2004. Low marine sulphate and protracted oxygenation of the Proterozoic biosphere. *Nature* 431, 834–838. <https://doi.org/10.1038/nature02974>.
- Kampschulte, A., Strauss, H., 2004. The sulfur isotopic evolution of Phanerozoic seawater based on the analysis of structurally substituted sulfate in carbonates. *Chem. Geol.* 204, 255–286. <https://doi.org/10.1016/j.chemgeo.2003.11.013>.
- Kampschulte, A., Bruckschen, P., Strauss, H., 2001. The Sulphur isotopic composition of trace sulphates in Carboniferous brachiopods: implications for coeval seawater, correlation with other geochemical cycles and isotope stratigraphy. *Chem. Geol.* 175, 149–173. [https://doi.org/10.1016/S0009-2541\(00\)00367-3](https://doi.org/10.1016/S0009-2541(00)00367-3).
- Kaplan, I.R., Emery, K.O., Rittenberg, S.C., 1963. The distribution and Isotopic Abundance of Sulphur in recent Marine Sediments off Southern California. *Geochim. Cosmochim. Acta* 27, 297. [https://doi.org/10.1016/0016-7037\(63\)90074-7](https://doi.org/10.1016/0016-7037(63)90074-7).
- Kump, L.R., Arthur, M.A., 1999. Interpreting carbon-isotope excursions: carbonates and organic matter. *Chem. Geol.* 161, 181–198. [https://doi.org/10.1016/S0009-2541\(99\)00086-8](https://doi.org/10.1016/S0009-2541(99)00086-8).
- Kwon, H., Woo, J., Oh, J.-R., Joo, Y.J., Lee, S., Nakrem, H.A., Sim, M.S., 2022. Responses of the biogeochemical sulfur cycle to early Permian tectonic and climatic events. *Earth Planet. Sci. Lett.* 591, 117604 <https://doi.org/10.1016/j.epsl.2022.117604>.
- Lawrence, M.G., Greig, A., Collerson, K.D., Kamber, B.S., 2006. Rare Earth Element and Yttrium Variability in South East Queensland Waterways. *Aquat. Geochem.* 12, 39–72. <https://doi.org/10.1007/s10498-005-4471-8>.
- Leu, M., Bucher, H., Goudemand, N., 2019. Clade-dependent size response of conodonts to environmental changes during the late Smithian extinction. *Earth Sci. Rev.* 195, 52–67. <https://doi.org/10.1016/j.earscirev.2018.11.003>.
- Leu, M., Bucher, H., Vennemann, T., Bagherpour, B., Ji, C., Brosse, M., Goudemand, N., 2022. A Unitary Association-based conodont biozonation of the Smithian–Spathian boundary (Early Triassic) and associated biotic crisis from South China. *Swiss J. Palaeontol.* 141, 19. <https://doi.org/10.1186/s13358-022-00259-x>.
- Leu, M., Bucher, H., Baud, A., Vennemann, T., Luz, Z., Hautmann, M., Goudemand, N., 2023. An expanded Smithian–Spathian (Lower Triassic) boundary from a reefal build-up record in Oman: implications for conodont taxonomy, high-resolution biochronology and the carbon isotope record. *Pap. Palaeontol.* 9, e1481 <https://doi.org/10.1002/spp2.1481>.
- Liu, X.-M., Kah, L.C., Knoll, A.H., Cui, H., Wang, C., Bekker, A., Hazen, R.M., 2021. A persistently low level of atmospheric oxygen in Earth’s middle age. *Nat. Commun.* 12, 351. <https://doi.org/10.1038/s41467-020-20484-7>.
- Lowenstein, T.K., Hardie, L.A., Timofeeff, M.N., Demicco, R.V., 2003. Secular variation in seawater chemistry and the origin of calcium chloride basinal brines. *Geology* 31, 857–860. <https://doi.org/10.1130/G19728R.1>.
- Luo, G., Kump, L.R., Wang, Y., Tong, J., Arthur, M.A., Yang, H., Huang, J., Yin, H., Xie, S., 2010. Isotopic evidence for an anomalously low oceanic sulfate concentration following end-Permian mass extinction. *Earth Planet. Sci. Lett.* 300, 101–111. <https://doi.org/10.1016/j.epsl.2010.09.041>.
- Lyons, T.W., Walter, L.M., Gellatly, A.M., Martini, A.M., Blake, R.E., 2004. Sites of anomalous organic remineralization in the carbonate sediments of South Florida, USA: The sulfur cycle and carbonate-associated sulfate. In: Amend, J.P., Edwards, K. J., Lyons, T.W. (Eds.), *Sulfur Biogeochemistry - Past and Present*. Geological Society of America, 0.

- Lyu, Z., Zhang, L., Algeo, T.J., Zhao, L., Chen, Z.-Q., Li, C., Ma, B., Ye, F., 2019. Global-ocean circulation changes during the Smithian–Spathian transition inferred from carbon-sulfur cycle records. *Earth Sci. Rev.* 195, 114–132. <https://doi.org/10.1016/j.earscirev.2019.01.010>.
- Marengo, P.J., Corsetti, F.A., Kaufman, A.J., Bottjer, D.J., 2008. Environmental and diagenetic variations in carbonate associated sulfate: an investigation of CAS in the lower Triassic of the western USA. *Geochim. Cosmochim. Acta* 72, 1570–1582. <https://doi.org/10.1016/j.gca.2007.10.033>.
- Millero, F.J., 2013. *Chemical Oceanography*, 4th ed. CRC Press.
- Mizutani, Y., Rafter, T.A., 1973. Isotopic behaviour of sulphate oxygen in the bacterial reduction of sulphate. *Geochem. J.* 6, 183–191. <https://doi.org/10.2343/geochemj.6.183>.
- Newton, R.J., Pevitt, E.L., Wignall, P.B., Bottrell, S.H., 2004. Large shifts in the isotopic composition of seawater sulphate across the Permo–Triassic boundary in northern Italy. *Earth Planet. Sci. Lett.* 218, 331–345. [https://doi.org/10.1016/S0012-821X\(03\)00676-9](https://doi.org/10.1016/S0012-821X(03)00676-9).
- Orchard, M.J., 2007. Conodont diversity and evolution through the latest Permian and early Triassic upheavals. *Palaeogeogr. Palaeoclimatol. Palaeoecol.* 252, 93–117. <https://doi.org/10.1016/j.palaeo.2006.11.037>.
- Ovtcharova, M., Bucher, H., Schaltegger, U., Galfetti, T., Brayard, A., Guex, J., 2006. New early to Middle Triassic U–Pb ages from South China: Calibration with ammonoid biochronozones and implications for the timing of the Triassic biotic recovery. *Earth Planet. Sci. Lett.* 243, 463–475. <https://doi.org/10.1016/j.epsl.2006.01.042>.
- Paris, G., Fehrenbacher, J.S., Sessions, A.L., Spero, H.J., Adkins, J.F., 2014. Experimental determination of carbonate-associated sulfate  $\delta^{34}\text{S}$  in planktonic foraminifera shells. *Geochem. Geophys. Geosyst.* 15, 1452–1461. <https://doi.org/10.1002/2014GC005295>.
- Payne, J.L., Lehrmann, D.J., Wei, J., Orchard, M.J., Schrag, D.P., Knoll, A.H., 2004. Large Perturbations of the Carbon Cycle during Recovery from the End-Permian Extinction. *Science* 305, 506–509. <https://doi.org/10.1126/science.1097023>.
- Paytan, A., Kastner, M., Campbell, D., Thiemens, M.H., 1998. Sulfur Isotopic Composition of Cenozoic Seawater Sulfate. *Science* 282, 1459–1462. <https://doi.org/10.1126/science.282.5393.1459>.
- Present, T.M., Paris, G., Burke, A., Fischer, W.W., Adkins, J.F., 2015. Large Carbonate Associated Sulfate isotopic variability between brachiopods, micrite, and other sedimentary components in late Ordovician strata. *Earth Planet. Sci. Lett.* 432, 187–198. <https://doi.org/10.1016/j.epsl.2015.10.005>.
- Present, T.M., Adkins, J.F., Fischer, W.W., 2020. Variability in sulfur isotope records of phanerozoic seawater sulfate. *Geophys. Res. Lett.* 47 <https://doi.org/10.1029/2020GL088766> e2020GL088766.
- Rennie, V.C.F., Paris, G., Sessions, A.L., Abramovich, S., Turchyn, A.V., Adkins, J.F., 2018. Cenozoic record of  $\delta^{34}\text{S}$  in foraminiferal calcite implies an early Eocene shift to deep-ocean sulfide burial. *Nat. Geosci.* 11, 761–765. <https://doi.org/10.1038/s41561-018-0200-y>.
- Romano, C., Goudebrand, N., Vennemann, T.W., Ware, D., Schneebeli-Hermann, E., Hochuli, P.A., Brühwiler, T., Brinkmann, W., Bucher, H., 2013. Climatic and biotic upheavals following the end-Permian mass extinction. *Nat. Geosci.* 6, 57–60. <https://doi.org/10.1038/ngeo1667>.
- Schobben, M., Stebbins, A., Ghaderi, A., Strauss, H., Korn, D., Korte, C., 2016. Eutrophication, microbial-sulfate reduction and mass extinctions. *Commun. Integr. Biol.* 9, e1115162 <https://doi.org/10.1080/19420889.2015.1115162>.
- Schreurs, G., Immenhauser, A., 1999. West-northwest directed obduction of the Batain Group on the eastern Oman continental margin at the Cretaceous-Tertiary boundary. *Tectonics* 18, 148–160. <https://doi.org/10.1029/1998TC900020>.
- Sedlacek, A.R., Saltzman, M.R., Algeo, T.J., Horacek, M., Brandner, R., Foland, K., Denniston, R.F., 2014.  $87\text{Sr}/86\text{Sr}$  stratigraphy from the early Triassic of Zal, Iran: linking temperature to weathering rates and the tempo of ecosystem recovery. *Geology* 42, 779–782.
- Shen, J., Algeo, T.J., Planayasky, N.J., Yu, J.X., Feng, Q.L., Song, H.J., Song, H.Y., Rowe, H., Zhou, L., Chen, J.B., 2019. Mercury enrichments provide evidence of early Triassic volcanism following the end-Permian mass extinction. *Earth Sci. Rev.* 195, 191–212. <https://doi.org/10.1016/j.earscirev.2019.05.010>.
- Song, H., Tong, J., Algeo, T.J., Horacek, M., Qiu, H., Song, H., Tian, L., Chen, Z.-Q., 2013. Large vertical  $\delta^{13}\text{C}_{\text{DIC}}$  gradients in early Triassic seas of the South China craton: Implications for oceanographic changes related to Siberian Traps volcanism. *Glob. Planet. Chang.* 105, 7–20. <https://doi.org/10.1016/j.gloplacha.2012.10.023>.
- Song, H., Tong, J., Algeo, T.J., Song, H., Qiu, H., Zhu, Y., Tian, L., Bates, S., Lyons, T.W., Luo, G., Kump, L.R., 2014. Early Triassic seawater sulfate drawdown. *Geochim. Cosmochim. Acta* 128, 95–113. <https://doi.org/10.1016/j.gca.2013.12.009>.
- Song, H., Wignall, P.B., Tong, J., Song, H., Chen, J., Chu, D., Tian, L., Luo, M., Zong, K., Chen, Y., Lai, X., Zhang, K., Wang, H., 2015. Integrated Sr isotope variations and global environmental changes through the late Permian to early late Triassic. *Earth Planet. Sci. Lett.* 424, 140–147. <https://doi.org/10.1016/j.epsl.2015.05.035>.
- Song, H., Du, Y., Algeo, T.J., Tong, J., Owens, J.D., Song, H., Tian, L., Qiu, H., Zhu, Y., Lyons, T.W., 2019. Cooling-driven oceanic anoxia across the Smithian/Spathian boundary (mid-early Triassic). *Earth Sci. Rev.* 195, 133–146. <https://doi.org/10.1016/j.earscirev.2019.01.009>.
- Spangenberg, J.E., Saintilan, N.J., Palinkas, S.S., 2022. Safe, accurate, and precise sulfur isotope analyses of arsenides, sulfarsenides, and arsenic and mercury sulfides by conversion to barium sulfate before EA/IRMS. *Anal. Bioanal. Chem.* 414, 2163–2179. <https://doi.org/10.1007/s00216-021-03854-y>.
- Stanley, S.M., 2007. An Analysis of the history of Marine Animal Diversity. *Paleobiology* 33, 1–55.
- Stanley, S.M., 2008. Predation defeats competition on the seafloor. *Paleobiology* 34, 1–21. <https://doi.org/10.1666/07026.1>.
- Stanley, S.M., 2009. Evidence from ammonoids and conodonts for multiple early Triassic mass extinctions. *Proc. Natl. Acad. Sci.* 106, 15264–15267. <https://doi.org/10.1073/pnas.0907992106>.
- Stebbins, A., Algeo, T.J., Krystyn, L., Rowe, H., Brookfield, M., Williams, J., Nye Jr., S.W., Hannigan, R., 2019a. Marine sulfur cycle evidence for upwelling and eutrophic stresses during early Triassic cooling events. *Earth Sci. Rev.* 195, 68–82. <https://doi.org/10.1016/j.earscirev.2018.09.007>.
- Stebbins, A., Algeo, T.J., Olsen, C., Sano, H., Rowe, H., Hannigan, R., 2019b. Sulfur-isotope evidence for recovery of seawater sulfate concentrations from a PTB minimum by the Smithian-Spathian transition. *Earth Sci. Rev.* 195, 83–95. <https://doi.org/10.1016/j.earscirev.2018.08.010>.
- Strauss, H., 1993. The sulfur isotopic record of Precambrian sulfates: new data and a critical evaluation of the existing record. *Precambrian Res.* 63, 225–246. [https://doi.org/10.1016/0301-9268\(93\)90035-Z](https://doi.org/10.1016/0301-9268(93)90035-Z).
- Strauss, H., 1997. The isotopic composition of sedimentary sulfur through time. *Palaeogeogr. Palaeoclimatol. Palaeoecol.* 132, 97–118. [https://doi.org/10.1016/S0031-0182\(97\)00667-9](https://doi.org/10.1016/S0031-0182(97)00667-9).
- Sun, Y.D., Wignall, P.B., Joachimski, M.M., Bond, D.P.G., Grasby, S.E., Sun, S., Yan, C.B., Wang, L.N., Chen, Y.L., Lai, X.L., 2015. High amplitude redox changes in the late Early Triassic of South China and the Smithian–Spathian extinction. *Palaeogeogr. Palaeoclimatol. Palaeoecol.* 427, 62–78. <https://doi.org/10.1016/j.palaeo.2015.03.038>.
- Taylor, S.R., McLennan, S.M., 1985. *The Continental Crust: Its Composition and Evolution*.
- Thomazo, C., Brayard, A., Elmeknessi, S., Vennin, E., Olivier, N., Caravaca, G., Escarguel, G., Fara, E., Bylund, K.G., Jenks, J.F., Stephen, D.A., Killingsworth, B., Sansjofre, P., Cartigny, P., 2019. Multiple sulfur isotope signals associated with the late Smithian event and the Smithian/Spathian boundary. *Earth Sci. Rev.* 195, 96–113. <https://doi.org/10.1016/j.earscirev.2018.06.019>.
- Toyama, K., Paytan, A., Sawada, K., Hasegawa, T., 2020. Sulfur isotope ratios in co-occurring barite and carbonate from Eocene sediments: a comparison study. *Chem. Geol.* 535, 119454 <https://doi.org/10.1016/j.chemgeo.2019.119454>.
- Turchyn, A.V., DePaolo, D.J., 2019. Seawater Chemistry through Phanerozoic Time. *Ann. Rev. Earth Planet. Sci.* 47, 197–224. <https://doi.org/10.1146/annurev-earth-082517-010305>.
- Vérard, C., 2019. Panalexis: towards global synthetic palaeogeographies using integration and coupling of manifold models. *Geol. Mag.* 156, 320–330. <https://doi.org/10.1017/S0016756817001042>.
- Walker, J.C.G., 1986. Global geochemical cycles of carbon, sulfur and oxygen. *Mar. Geol.* 70, 159–174. [https://doi.org/10.1016/0025-3227\(86\)90093-9](https://doi.org/10.1016/0025-3227(86)90093-9).
- Widmann, P.A., 2019. Temporal Calibration and Quantification of Early Triassic Climatic Disturbances through High-Precision U–Pb Zircon Dating and an Improved Chemical Abrasion Procedure. *Département des sciences de la Terre. Université de Genève, Genève.* <https://doi.org/10.13097/archive-ouverte/unige:121676>.
- Widmann, P., Bucher, H., Leu, M., Vennemann, T., Bagherpour, B., Schneebeli-Hermann, E., Goudebrand, N., Schaltegger, U., 2020. Dynamics of the largest carbon isotope excursion during the early Triassic biotic recovery. *Front. Earth Sc.-Switz.* 196 <https://doi.org/10.3389/feart.2020.00196>.
- Witts, J.D., Newton, R.J., Mills, B.J.W., Wignall, P.B., Bottrell, S.H., Hall, J.L.O., Francis, J.E., Alistair Crame, J., 2018. The impact of the Cretaceous–Paleogene (K–Pg) mass extinction event on the global sulfur cycle: Evidence from Seymour Island, Antarctica. *Geochim. Cosmochim. Acta* 230, 17–45. <https://doi.org/10.1016/j.gca.2018.02.037>.
- Wortmann, U.G., Bernasconi, S.M., Böttcher, M.E., 2001. Hypersulfidic deep biosphere indicates extreme sulfur isotope fractionation during single-step microbial sulfate reduction. *Geology* 29, 647–650. [https://doi.org/10.1130/0091-7613\(2001\)029<0647:HDBIES>2.0.CO;2](https://doi.org/10.1130/0091-7613(2001)029<0647:HDBIES>2.0.CO;2).
- Wotte, T., Shields-Zhou, G.A., Strauss, H., 2012. Carbonate-associated sulfate: Experimental comparisons of common extraction methods and recommendations toward a standard analytical protocol. *Chem. Geol.* 326–327, 132–144. <https://doi.org/10.1016/j.chemgeo.2012.07.020>.
- Zhang, L., Zhao, L., Chen, Z.Q., Algeo, T.J., Li, Y., Cao, L., 2015. Amelioration of marine environments at the Smithian-Spathian boundary, early Triassic. *Biogeosciences* 12, 1597–1613. <https://doi.org/10.5194/bg-12-1597-2015>.
- Zhang, F., Romaniello, S.J., Algeo, T.J., Lau, K.V., Clapham, M.E., Richoz, S., Herrmann, A.D., Smith, H., Horacek, M., Anbar, A.D., 2018. Multiple episodes of extensive marine anoxia linked to global warming and continental weathering following the latest Permian mass extinction. *Sci. Adv.* 4, e1602921 <https://doi.org/10.1126/sciadv.1602921>.
- Zhang, F., Algeo, T.J., Cui, Y., Shen, J., Song, H., Sano, H., Rowe, H.D., Anbar, A.D., 2019. Global-ocean redox variations across the Smithian-Spathian boundary linked to concurrent climatic and biotic changes. *Earth Sci. Rev.* 195, 147–168.